

HARD X-RAY EMITTING ACTIVE GALACTIC NUCLEI SELECTED BY THE *CHANDRA* MULTI-WAVELENGTH PROJECT

J. D. SILVERMAN^{1,2,3}, P. J. GREEN⁴, W. A. BARKHOUSE, D.-W. KIM, T. L. ALDCROFT, R. A. CAMERON, B. J. WILKES,
A. MOSSMAN, H. GHOSH, H. TANANBAUM

Harvard-Smithsonian Center for Astrophysics, 60 Garden Street, Cambridge, MA 02138

M. G. SMITH, R. C. SMITH

Cerro Tololo Inter-American Observatory, National Optical Astronomical Observatory, Casilla 603, La Serena, Chile

P. S. SMITH

Steward Observatory, The University of Arizona, Tucson, AZ 85 721

C. FOLTZ

National Science Foundation, 4201 Wilson Blvd., Arlington, VA, 22230

D. WIK

Astronomy Department, University of Virginia, P.O. Box 3818, Charlottesville, VA, 22903-0818

AND

B. T. JANNUZI

National Optical Astronomical Observatory, P.O. Box 26732, Tucson, AZ, 85726-6732

To appear in The Astrophysical Journal

ABSTRACT

We present X-ray and optical analysis of 188 AGN identified from 497 hard X-ray ($f_{2.0-8.0\text{keV}} > 2.7 \times 10^{-15} \text{ erg cm}^{-2} \text{ s}^{-1}$) sources in 20 *Chandra* fields (1.5 deg^2) forming part of the *Chandra* Multi-wavelength Project. These medium depth X-ray observations enable us to detect a representative subset of those sources responsible for the bulk of the 2–8 keV Cosmic X-ray Background. Brighter than our optical spectroscopic limit, we achieve a reasonable degree of completeness (77% of X-ray sources with counter-parts $r' < 22.5$ have been classified): broad emission line AGN (62%), narrow emission line galaxies (24%), absorption line galaxies (7%), stars (5%) or clusters (2%). We find that most X-ray unabsorbed AGN ($N_{\text{H}} < 10^{22} \text{ cm}^{-2}$) have optical properties characterized by broad emission lines and blue colors, similar to optically-selected quasars from the Sloan Digital Sky Survey but with a slightly broader color distribution. However, we also find a significant population of redder ($g'-i' > 1.0$) AGN with broad optical emission lines. Most of the X-ray absorbed AGN ($10^{22} < N_{\text{H}} < 10^{24} \text{ cm}^{-2}$) are associated with narrow emission line galaxies, with red optical colors characteristically dominated by luminous, early type galaxy hosts rather than from dust reddening of an AGN. We also find a number of atypical AGN; for instance, several luminous AGN show both strong X-ray absorption ($N_{\text{H}} > 10^{22} \text{ cm}^{-2}$) and broad emission lines. Overall, we find that 81% of X-ray selected AGN can be easily interpreted in the context of current AGN unification models. Most of the deviations seem to be due to an optical contribution from the host galaxies of the low luminosity AGN.

Subject headings: X-rays: galaxies — galaxies: active — quasars: general — surveys

1. INTRODUCTION

In the era of *Chandra* and *XMM-Newton*, X-ray surveys of the extragalactic universe are for the first time able to probe the demographics and evolution of the AGN population irrespective of any moderate ob-

scuration. Current deep surveys such as the CDF-N (Barger et al. 2002), CDF-S (Tozzi et al. 2001) and the Lockman Hole (Mainieri et al. 2002) are unveiling both bright quasars and lower luminosity Seyfert galaxies with significant absorbing gas columns. This obscuration can be large enough to effectively hide any optical signature of an active nucleus. With the unprecedented sensitivity and resolving power of these current observatories, we are able to probe large volumes to determine the prevalence of X-ray emitting AGN and their evolution.

The study of AGN enshrouded by dust and gas is not new. Obscured AGN (e.g., narrow line radio galaxies, Seyfert 2s, IRAS sources) have been under investigation for many years, though a complete census of the popu-

¹ Astronomy Department, University of Virginia, P.O. Box 3818, Charlottesville, VA, 22903-0818

² Visiting Astronomer, Kitt Peak National Observatory and Cerro Tololo Inter-American Observatory, National Optical Astronomy Observatory, which is operated by the Association of Universities for Research in Astronomy, Inc. (AURA) under cooperative agreement with the National Science Foundation.

³ jsilverman@cfa.harvard.edu

⁴ pgreen@cfa.harvard.edu

lation has been out of reach. The spectrum of the Cosmic X-ray Background (CXRB) has provided evidence of the preponderance of the hidden AGN population. While *ROSAT* has shown that unabsorbed AGN dominate the soft (0.1–2 keV) CXRB (Hasinger et al. 1998), its high energy spectrum (2–30 keV) is harder than that of known AGN. Models based on the CXRB spectrum and the X-ray luminosity function have predicted the existence of large numbers of heavily obscured AGN that have been missed in past surveys (Comastri et al. 1995; Gilli et al. 2001).

How do these sources fit into the AGN unification scheme (e.g., Antonucci 1993; Antonucci & Miller 1985)? Many of the absorbed X-ray sources lack optical AGN signatures (e.g. Barger et al. 2003). Is this a result of host dilution (Moran, Filippenko & Chornock 2002) or some other geometry/structure that prevents us from viewing the emission line gas? While optical extinction and X-ray absorption are statistically correlated (Smith & Done 1996; Turner et al. 1997), there are a number of counter examples. X-ray observations of Seyfert 2 galaxies do not always provide evidence for a large intrinsic obscuring column (Panessa & Bassani 2002; Georgantopoulos & Zezas 2003). Equally compelling, a number of X-ray selected type 1 AGN (Mainieri et al. 2002; Akylas et al. 2003) have significant intrinsic absorption in the X-ray band ($10^{20} < N_{\text{H}} < 10^{23} \text{ cm}^{-2}$). Wilkes et al. (2002) find that a large fraction of the IR selected AGN found in the Two-Micron All Sky Survey (2MASS) have broad optical emission lines and a wide range of X-ray absorption. Given the complex environment of some of these AGN, one line of sight might not always exemplify the overall geometry.

While the *Chandra* and *XMM-Newton* deep fields do cover a large volume, wide field surveys are needed to compile a significant sample of sources with 2–8 keV flux levels around $10^{-15} - 10^{-14} \text{ erg cm}^{-2} \text{ s}^{-1}$. Such sources comprise most of the flux of the 2–8 keV CXRB (Moretti et al. 2003; Cowie et al. 2002). The deep fields provide relatively few sources at these flux levels to characterize the absorbed AGN population. Many ongoing surveys at intermediate flux levels are currently contributing to our understanding of the X-ray emitting AGN. For example, the HELLAS2XMM (Fiore et al. 2003) and XMM/SSC (Barcons et al. 2003) take advantage of the large field of view and high collecting area of *XMM-Newton*. The SEXSI (Harrison et al. 2003) survey joins the *Chandra* Multi-wavelength Project in utilizing *Chandra*'s small PSF and low background to detect the faint AGN and unambiguously find optical counter-parts. With large samples of all AGN types, we can characterize the dominant population contributing to the CXRB and determine the relative importance and nature of interesting AGN that defy a simple unification model.

2. THE *CHANDRA* MULTI-WAVELENGTH PROJECT (CHAMP)

The ChaMP (Kim et al. 2004a; Kim et al. 2004b; Green et al. 2004) is providing a medium-depth, wide-area survey of serendipitous X-ray sources from archival *Chandra* fields covering $\sim 14 \text{ deg}^2$. The broadband sensitivity between 0.3–8.0 keV enables the selection to be far less affected by absorption than previous optical, UV,

or soft X-ray surveys. *Chandra*'s small point spread function ($\sim 1''$ resolution on-axis) and low background allow sources to be detected to fainter flux levels, while the $\sim 1''$ X-ray astrometry greatly facilitates unambiguous optical identification of X-ray counter-parts. The project effectively bridges the gap between flux limits achieved with the *Chandra* deep field observations and those of past *ROSAT* and *ASCA* surveys. A total of about 8000 serendipitous extragalactic X-ray sources are expected when the project is complete. A primary aim of the ChaMP is to measure the luminosity function of quasars and lower luminosity AGN out to $z \sim 4$ with the inclusion of the obscured population (J.D. Silverman et al. 2004, in preparation).

We present results from the ChaMP using a subsample ($f_{2.0-8.0\text{keV}} > 2.7 \times 10^{-15} \text{ erg cm}^{-2} \text{ s}^{-1}$ and $r' < 22.5$) of 497 X-ray sources detected in the hard band (2.5–8.0 keV) in 20 fields. This work is an extension of the 6 fields analyzed by Green et al. (2004), here limited to the hard X-ray band. From this subsample, we classify 188 as AGN based on their X-ray luminosity ($L_{2-8 \text{ keV}} > 10^{42} \text{ erg s}^{-1}$). Our motivation is to determine the demographics of the hard X-ray emitting AGN, measure the range of intrinsic obscuration, and determine the extent to which obscuration of X-rays translates to extinction in the optical. After briefly discussing the X-ray and optical data acquisition, reduction and analysis (§3 & §4), we describe the characteristics of the hard X-ray sources (§5) and the AGN properties (§6) including selection and completeness. In section §7, we present the results. Throughout this paper, we assume $H_0 = 70 \text{ km s}^{-1} \text{ Mpc}^{-1}$, $\Omega_{\Lambda} = 0.7$, and $\Omega_{\text{M}} = 0.3$.

3. X-RAY OBSERVATIONS

We have chosen 20 *Chandra* fields (Table 1) for which we have acquired extensive followup optical imaging and spectroscopy. These fields have been selected from the first two years of *Chandra* archival data. Only ACIS observations at high galactic latitude ($|b| > 20^\circ$) with no special observing modes (e.g., gratings) are used. The deepest observations have exposure times that are sensitive to sources with $f_{2-8\text{keV}} > 2 \times 10^{-15} \text{ erg cm}^{-2} \text{ s}^{-1}$. At this flux limit, we resolve $\sim 70\%$ of the 2–8 keV CXRB (Moretti et al. 2003; Figure 5). The target of each observation has been excluded to avoid any bias towards specific objects such as AGNs associated with clusters.

A full description of the ChaMP image reduction and analysis pipeline XPIPE can be found in Kim et al. (2004a). In short, we have an automated reduction routine that filters out high background intervals, bad events such as cosmic rays and hot pixels to produce a clean and robust X-ray source catalog. Source extraction is performed using a wavelet detection algorithm (CIAO/*wavdetect*; Freeman et al. 2002) in three energy bands (Broad (B): 0.3–8.0 keV, Soft (S): 0.3–2.5 keV, Hard (H): 2.5–8.0 keV).

For the following analysis, we require a S/N > 2 in the 2.5–8.0 keV band to generate a hard X-ray selected sample which minimizes any inherent bias against the absorption of soft X-rays. We restrict the off-axis angle of the detections to less than $12'$ since the sensitivity beyond this is significantly reduced. We do not use chip S4 (ccd_id=8) since this CCD is severely affected by a flaw in the serial readout, causing a significant amount of charge

to be randomly deposited along pixel rows as they are read out. Each detection has a unique effective exposure time which includes vignetting. The conversion from X-ray count rate to flux units ($\text{erg cm}^{-2} \text{s}^{-1}$) is determined from simulated detections on each CCD of a source with a powerlaw spectrum ($f_E \propto E^{-(\Gamma-1)}$; $\Gamma = 1.7^5$) and galactic absorption (Dickey & Lockman 1990). The effect of varying the photon index (Γ) from 1.7 to 1.9 results in a $\sim 2\%$ difference in flux for both ACIS-I and ACIS-S. We calculate the flux in the conventional 2.0–8.0 keV band for comparison with other surveys.

With *Chandra*'s broad band sensitivity (0.3–8.0 keV), we are able to investigate the spectral properties of the sample, though we are limited by the small number of source counts in most cases (90% of sources have $9 < \text{counts} < 70$ in the 2.0–8.0 keV band). The hardness ratio ($\text{HR} = \text{H-S}/\text{H+S}$) can be used as a crude assessment of the spectral characteristics. Since the response of *Chandra* varies as a function of energy and off-axis angle with the additional complication of mixing frontside and backside illuminated CCDs, we have converted the raw HR to an effective, on-axis, ACIS-I value by multiplying the count rate in each band by the ratio of the ECF (off-axis CCD) to the on-axis ECF which ranges between 0.6–2.0.

3.1. X-ray spectral fits

X-ray spectral modeling provides a robust way of characterizing the spectral properties of our sample, independent of observation and instrument details. With a measured redshift, we can more accurately determine the intrinsic absorbing column than that based solely on hardness ratios. Some objects that look soft in HR may have significant absorption especially at higher redshifts. For each X-ray source in our hard-selected sample, we use an automated procedure to extract the spectrum and fit a model to the data. Due to a lack of counts, we cannot usefully fit a spectral powerlaw model, leaving both spectral index and intrinsic absorbing column free for all objects.

All processing is done using CIAO 3.0.2⁶ and CALDB 2.26⁷. The detailed steps to prepare the PHA (Pulse-Height Analysis) spectrum follow. First, we define a circular region centered on the X-ray source sized to contain 95% of 1.5 keV photons at the given off-axis angle. The background region is annular with a width of 20'' centered on the source. We exclude any nearby sources from both the source and background regions. We then use CIAO tool *psextract* to create a PHA spectrum covering the energy range 0.4–8 keV. We generate both an ungrouped spectrum and one which is grouped to a minimum of 10 counts per channel. The time-dependent quantum efficiency degradation of ACIS is accounted for when the ARF is generated by the *mkarf* tool.

Spectral fitting is done using the CIAO *Sherpa*⁸ tool. For all sources, we fit an absorbed powerlaw containing an intrinsic absorber with neutral column N_{H} at the

source redshift. Our choice of photon index (Frozen at $\Gamma = 1.9$) is based on previous studies of unabsorbed AGN. Reeves & Turner (2000) have measured the spectral index for radio quiet AGN using *ASCA* observations to be $\Gamma \sim 1.9$. Piconcelli et al. (2003) have measured a mean photon index 1.8–1.9 with *XMM-Newton* which shows no variation over the redshift range $0 < z < 2$. This N_{H} fit provides a robust one-parameter characterization of the intrinsic spectral shape for as few as 10 counts. We verified by an extensive Monte-Carlo simulation that the parameter uncertainties calculated with *projection* of confidence contours in *Sherpa* are reliable. Note that the spectral model contains a fixed Galactic neutral absorber appropriate for each object. Spectra with at least 60 counts are fit using the grouped spectrum with the hybrid Monte-Carlo Levenberg-Marquardt minimization method, while the low count spectra are fit using the ungrouped data with Cash statistics and the Powell method. Spectra with over 200 counts are also fit with a two-parameter absorbed powerlaw leaving both Γ and the intrinsic N_{H} at the source redshift free to vary. The results from the two-parameter fitting are included in this paper for a couple of sources discussed in Section 7.2. The full analysis will be presented in an upcoming ChaMP paper (T.L. Aldcroft et al. 2004, in preparation).

4. OPTICAL FOLLOWUP

4.1. Imaging

We have acquired optical imaging for each *Chandra* field to identify counter-parts to X-ray sources. We use the NOAO Blanco and Mayall 4m telescopes and their MOSAIC cameras to image the full *Chandra* field-of-view of our survey fields. The exposure times are scaled from the minimum X-ray flux for a detection per *Chandra* field to identify $> 90\%$ of *ROSAT* AGN (Yuan et al. 1998). Three filters (g' , r' , i') using the Sloan Digital Sky Survey (SDSS) photometric system (Fukugita et al. 1996) are implemented to measure broad band colors for preliminary source classification. Table 2 provides some details of the imaging for the fourteen fields not included in Green et al. (2004).

A full description of the optical followup program including strategy, image reduction, source detection and photometric calibration can be found in (Green et al. 2004). Briefly, optical image reduction on the MOSAIC data is performed with the *mscred* (Valdes 2002) package within the IRAF⁹ environment. We use the SExtractor (Bertin & Arnouts 1996) algorithm to detect sources, and measure their positions and brightness. Since the X-ray source positions are only accurate to within $\sim 1''$, the optical astrometric solution is required to achieve the $\text{rms} < 0.3''$ accuracy necessary for spectroscopic followup. We require an accuracy of the photometric solution to less than a tenth of a magnitude. The majority of the AGN sample (88%) presented in this paper has magnitude errors less than 0.05 as a result of the bright optical magnitude selection. In addition, we find a mean color offset of 0.05 magnitudes to the red between our

⁵ The ChaMP XPIPE (Kim et al. 2004a) provides energy conversion factors (ECF) for two models with $\Gamma = 1.7$ and $\Gamma = 1.4$. We chose the former since the photon index more closely resembles the majority of the hard source detections.

⁶ <http://cxc.harvard.edu/ciao>

⁷ <http://cxc.harvard.edu/caldb>

⁸ <http://cxc.harvard.edu/sherpa>

⁹ IRAF is distributed by the National Optical Astronomy Observatory, which is operated by the Association of Universities for Research in Astronomy, Inc., under cooperative agreement with the National Science Foundation.

$g' - i'$ color and the SDSS using sources detected in both surveys.

4.2. X-ray to optical source matching

We implement an automated routine to match each X-ray source with potential optical counter-parts (see Green et al. 2004). The search radius is increased for X-ray detections at large off-axis angles. Each match is visually inspected and a confidence level is determined. For X-ray sources with multiple optical counter-parts, the optical source closest to the X-ray centroid is usually given a higher confidence. We have found 415 optical counter-parts to 497 X-ray sources (84%; Figure 1). We have not included 36 sources because the X-ray detection fell on a chip edge or there were multiple optical counter-parts for which no single optical source could confidently be assigned. We note that 81% of the matches have an X-ray to optical offset $< 2''$.

4.3. Spectroscopy

Optical spectroscopy is crucial for determining the source type and redshift. We acquired the majority of our optical spectra with the WIYN/3.5m and CTIO/4m with the HYDRA multi-fiber spectrographs, which have a field of view ($> 40'$) that fully covers the *Chandra* field. To extend spectroscopic classifications beyond $r' \sim 21$, the limit of the 4m class telescopes with HYDRA, we have obtained spectra from Magellan and the MMT. The field of view of Magellan with LDSS-2, a multi-slit spectrograph, is $5'$, so it takes 5–6 pointings to cover the full *Chandra* field. We have been using the FLWO 1.5m to acquire spectra of the optically bright ($r' < 17$) counter-parts. In addition, a number of people, mentioned in the acknowledgements, have graciously acquired long slit spectra of a few ChaMP sources during their own observing time. All redshifts have an accuracy of $\Delta z < 0.001$. Table 3 gives a summary of the spectroscopic facilities used by the ChaMP project.

We implement a classification scheme of optical spectra similar to the *Einstein Observatory* Extended Medium-Sensitivity Survey (Stocke et al. 1991). Objects with strong emission lines ($W_\lambda > 5 \text{ \AA}$) are classified as either Broad Line AGN (BLAGN; $\text{FWHM} > 1000 \text{ km s}^{-1}$) or Narrow Emission Line Galaxy (NELG; $\text{FWHM} < 1000 \text{ km s}^{-1}$). Counter-parts with weak emission line or pure absorption line spectra are classified as Absorption Line Galaxy (ALG). We note that there is a combination of redshift range and spectral bandpass for which we may lose important AGN optical diagnostic features. In some cases, the host galaxy contribution can prevent $H\beta$ from being a useful AGN indicator. Given the low signal-to-noise of our spectra, some NELG may have weak, broad emission lines. Ho et al. (1997) found that broad $H\alpha$ can often be found in low luminosity “dwarf” Seyferts with high S/N spectra and proper subtraction of the stellar continuum. This type of analysis is not possible given the quality of our spectra. Any stellar source is labelled as a STAR. For the ALG, we measure the Ca II break “CONTRAST” (Stocke et al. 1991) to look for a power-law AGN component to the continuum to note potential BL LAC candidates. If the associated X-ray emission is extended the object is further labelled as a possible cluster member.

As shown in Figure 1, we have classified 44% (220) of all the hard X-ray sources through our spectroscopic campaign. The sources without redshifts are primarily at faint optical magnitudes ($r' > 22$). In Table 4, we list the numbers of each type for various limits imposed on the sample.

5. CHARACTERISTICS OF THE HARD X-RAY SAMPLE

5.1. X-ray and optical flux

We show the optical magnitude (r') as a function of X-ray flux (2.0–8.0 keV) for the 497 sources detected in 20 fields (Figure 1). Lines of constant $f_X/f_{r'}$ are determined as follows.

$$\log(f_X/f_{r'}) = \log(f_X) + 0.4r' + 5.41 \quad (1)$$

This relation has been derived using an assumed powerlaw ($f_E \propto E^{-\alpha}$) with spectral index $\alpha_O = 0.5$ and $\alpha_X = 0.7$. The characteristics of the r' filter are taken from Fukugita et al. (1996). Most objects have $0.1 < f_X/f_{r'} < 10$. There exists a significant number of X-ray bright, optically faint sources ($f_X/f_{r'} > 10$), many of which are not detected in our optical imaging. Due to their optical faintness, we have only identified one such source, an NELG.

Based on the 210 spectroscopically identified objects with $r' < 22.5$, we find that 62% of the hard X-ray sources are classified as BLAGN. As shown in Green et al. (2004), these AGN tend to follow the relation $f_X = f_{r'}$ over a wide range of optical and X-ray flux. The NELG, which comprise 24% of the identifications, have flux ratios similar to the BLAGN. We find a number of counter-parts (7% ALG) that have no evidence for an emitting line region. These galaxies are primarily identified at bright optical magnitudes ($r' < 21$) due to the difficulty of classifying sources without strong emission lines at high redshift ($z > 0.5$). In addition, a few hard X-ray detected sources are associated with optically bright stars (5%) and galaxy clusters (2%) with extended X-ray emission.

5.2. X-ray spectral properties

The X-ray hardness ratio provides a crude measure of the spectral properties and classification of the hard X-ray sources. In Figure 2, we plot the corrected hardness ratio (Section 3) as a function of X-ray flux. The flux range shown includes all sources with the exception of the extremely bright cataclysmic variable TX Col (Schlegel & Salinas 2004). The horizontal lines mark the hardness ratio which corresponds to an X-ray source with a powerlaw continuum (photon index $\Gamma = 1.9$) absorbed by a column of gas at $z = 0$. Some of the derived N_H detections may be higher (see Section 3.1) using an absorber intrinsic to the source. According to Moretti et al. (2003), we are resolving $\sim 70\%$ of the full 2–8 keV CXRB at our chosen flux limit. With a flux weighted mean HR for the ChaMP sources of -0.39 , the X-ray spectrum of the ensemble is similar to the spectral characteristic of the integrated CXRB ($\Gamma=1.4$) which corresponds to a hardness ratio of -0.42 .

As described in many studies with *Chandra* (e.g., Mushotzky et al. 2000) and *XMM-Newton* (e.g., Hasinger et al. 2001), the X-ray source population becomes relatively harder at fainter flux levels. As evident in Figure 2, the hardest (HR >0) X-ray sources in

these ChaMP fields are predominately at $\log_{10}(f_X) < -13.6$. At fainter flux levels, the sources have a more even distribution over all hardness ratios. This spectral variation has been attributed to intrinsic absorption rather than changes in the intrinsic spectral energy distribution (Mainieri et al. 2003; Kim et al. 2004b). This will be further investigated in an upcoming ChaMP paper on the X-ray spectral properties of the AGN sample.

6. HARD AGN SAMPLE

6.1. Selection and completeness

In these medium depth *Chandra* fields, we are sensitive to X-ray sources with a 2.0–8.0 keV flux greater than 2.7×10^{-15} erg cm $^{-2}$ s $^{-1}$. The addition of a spectroscopic limit of $r' < 22.5$, yields a sample of X-ray sources which is 77% identified. This optical magnitude limit does bias the sample against optically faint counter-parts at the lower X-ray flux levels.

To construct a pure AGN sample, we require the rest frame 2.0–8.0 keV luminosity (uncorrected for intrinsic absorption) to exceed 10^{42} erg s $^{-1}$ thereby excluding any sources that may contain a significant stellar or hot ISM component. The most luminous known star-forming (Zezas et al. 2003; Lira et al. 2002) or elliptical (O’Sullivan, Forbes & Ponman 2001) galaxies attain at most $L_X = 10^{42}$ erg s $^{-1}$. Since many of the traditional optical AGN signatures are not present in obscured sources, high X-ray luminosity becomes our single discriminant for supermassive black hole accretion. We believe that almost all of the NELG and ALG harbor accreting SMBHs based on their X-ray luminosity. We find that 90% of the identified ChaMP sources have luminosities above this threshold. These selection criteria yield a sample of 188 AGN from 20 *Chandra* fields with $f_{2-8\text{keV}} > 2.7 \times 10^{-15}$ erg cm $^{-2}$ s $^{-1}$, $r' < 22.5$ and $L_X > 10^{42}$ erg s $^{-1}$. We have removed 5 objects identified as clusters based on their extended X-ray emission. A truncated version of the AGN catalog is presented in Table 5 and a full version is available in electronic form. This sample is composed of 69% BLAGN, 24% NELG and 7% ALG (Table 4).

6.2. Redshift and luminosity distribution

As shown in Figure 3, *Chandra* detects hard BLAGN out to $z \sim 4$ in these medium depth observations. In contrast, we have only identified non-BLAGN with $z < 0.8$. The steep drop in the number of NELG and ALG above this redshift is primarily due to an optical selection bias. The NELG and ALG lack prominent broad emission lines and may be resolved, having a magnitude fainter than our $r'=22.5$ limit within our spectroscopic aperture. Even a luminous host galaxy (10L $_{\star}$) at $z \sim 0.8$ is fainter than this limit. However, the *Chandra* Deep field surveys are finding a peak in the number distribution at $z \sim 0.8$ with a sharp dropoff beyond $z \sim 1$ (Cowie et al. 2003). Therefore, the peak in our distribution for NELG and ALG is unlikely to change drastically with the identification of the optically faint sources.

6.3. Low luminosity AGN and composite systems

Even though we have mitigated bias against obscured AGN by carrying out a hard X-ray survey, we still need to incorporate the optical properties of these AGN to

determine their nature and how they fit into the unification scheme. Many of the newly detected *Chandra* and *XMM-Newton* sources in the deep fields show no evidence for an AGN in the optical.

Optical emission from these low luminosity AGN can include a significant contribution from the host galaxy (Fiore et al. 2003; Green et al. 2004). This tends to be the case for AGN with $L_X < 10^{43}$ erg s $^{-1}$. We plot in Figure 4 the monochromatic, rest frame optical (2500 Å) versus X-ray (2 keV) luminosity density for our hard AGN sample with $f_{2-8\text{keV}} > 1 \times 10^{-14}$ erg cm $^{-2}$ s $^{-1}$ and $r' < 22.5$. We measure the optical luminosity density at 2500 Å from the r' magnitude as in Fukugita et al. (1996), assuming a powerlaw spectrum with $\alpha_O = 0.5$. The monochromatic X-ray luminosity is derived from the hard band flux using a powerlaw spectrum with $\alpha_X = 1.0$. The additional X-ray flux limit is imposed to include BLAGN across the full range of α_{OX} ($\sim 1 - 2$). If we included BLAGN with fainter X-ray fluxes, we would be biasing the sample too strongly towards optically bright objects based on our optical magnitude limit. The BLAGN above $\log \nu_L(2.0\text{ keV}) > 43.5$ share a similar X-ray to optical ratio ($< \alpha_{OX} > = 1.48 \pm 0.03$) while the lower luminosity AGN depart from this relation.

Most studies of X-ray selected AGN rely on optical spectroscopy for further classification. This can be misleading since it is difficult to isolate the nuclear region at these distances (Moran, Filippenko & Chornock 2002) with a $\sim 1''$ aperture. While most of the optical counter-parts of ChaMP sources have emission lines similar to quasars and lower luminosity Seyfert galaxies, limited wavelength coverage can cause some confusion with source classification as described by Page et al. (2003). For example, we display in Figure 5 two sources each with optical spectra spanning different wavelength ranges. Depending on the observed wavelength coverage, the classification can change drastically with the detection of broad emission lines either at the blue end of the spectrum (Src # 35; Mg II) or the red end (Src #42; H α). However, the inclusion of these AGN in our sample highlight the power of X-ray selection to reveal supermassive black hole accretion even under a veil of obscuration or host contamination.

6.4. Comparison with the optically selected samples (SDSS)

With optical imaging in three SDSS bands (g' , r' , i'), the SDSS becomes the easiest and largest sample of AGN to which we can compare our ChaMP AGN. The second edition of the SDSS quasar catalog (Schneider et al. 2003) contains 16,713 objects with $M_{i'} < -22$ out to $z = 5.41$ from the first public data release. We have selected 10,736 of these which were targeted as quasars solely based on their optical colors (BEST spectroscopic flag=1 for either low- z and high- z quasars). In Figure 6a, we have plotted the optical color ($g'-i'$) of the ChaMP AGN and the quasars from the SDSS as a function of redshift. Following Richards et al. (2001), we have measured the color offset (Figure 6b) from the median color of type 1 quasars from the SDSS.

The ChaMP BLAGN follow the color locus of SDSS quasars (Figure 6) for $z > 1$. The ChaMP BLAGN are slightly redder with a color excess of 0.1 magnitudes

compared to the median SDSS quasar colors (Figure 7). Given the photometric accuracy (0.1 mag) of ChaMP, we cannot with strong confidence report a difference of the mean between the two samples, though we probably achieve a higher precision with our sample of 95 ChaMP BLAGN. We do find a 0.03% likelihood that the color distribution of the ChaMP BLAGN ($z > 1$; $M_{i'} < -22$) can be drawn from the SDSS quasar population using a Kolmogorov-Smirnov test (Press et al. 1992). In Figure 7, we see that the ChaMP BLAGN have a wider color distribution ($\sigma_{\Delta g'-i'}=0.41$) than the SDSS quasars ($\sigma_{\Delta g'-i'}=0.26$). Besides the width of the distribution, we can compare the symmetry about the mean by measuring the skewness of the distribution, defined in Equation 2.

$$skewness = \frac{\sum_{i=1}^N (y_i - \bar{y})^3}{(N-1)\sigma^3} \quad (2)$$

We find that the distribution of ChaMP BLAGN has a red wing (skewness=-1.7) which causes the mean to shift further to the red than the SDSS quasars (skewness=7.1). We calculate that 26% of our ChaMP AGN sample has $\Delta g'-i' > 0.2$ above that expected from the SDSS distribution. Therefore, an X-ray selected sample can reveal a population of luminous, red AGN underrepresented in optically selected samples. At $z < 1$ (Figure 6), we see a population of red BLAGN that would not be detected in the SDSS. As shown in Figure 8a, these red BLAGN tend to have low optical luminosities ($M_{i'} < -24$) and are probably missed in the SDSS due to their continuum color, which can be influenced by their host galaxy. In Figure 8b, we see that many of the red BLAGN are below the flux limit of the SDSS. A larger sample of optically bright ChaMP AGN is required to definitively identify a population missed by the optical surveys.

Most ChaMP NELG and ALG are red and fall off the color range for optically selected type 1 quasars. We would not expect these types of AGN to be included in the SDSS quasar catalog due to their narrow or nonexistent emission lines and most have $M_{i'} > -22$. These objects appear to have colors dominated by their host galaxy. To illustrate, we plot in Figure 6a the expected colors of an elliptical (E0) and a spiral (Sb) galaxy using the Hyper_z (Bolzonella, Miralles, & Pell 2000) photometric code. We have assumed a Bruzual-Charlot spectral energy distribution, galactic extinction ($E_{B-V}=0.05$) using the Calzetti (1999) reddening law and no intrinsic dust reddening. Most NELG and ALG have colors between these two tracks. We also plot the type 2 SDSS QSO candidates from Zakamska et al. (2003). The absolute magnitude ($M_{i'}$) is calculated from the i^* magnitude with a correction for Galactic extinction ($E_{B-V}=0.05$) and no k -correction. The ChaMP NELG and SDSS type 2 QSOs potentially represent the same population. The extraordinary advantage of an X-ray selected survey is seen with the detection of AGN with no optical emission lines at all (ALG).

7. X-RAY ABSORPTION AND OPTICAL EXTINCTION

We present evidence of a direct relationship between the absorption of X-rays and optical extinction for the majority of the hard AGN, as expected if unification models (Antonucci 1993) extend to the X-ray regime. We attempt to reconcile the variety of AGN types from

an X-ray perspective. We use the term absorbed for any AGN with X-ray $N_H > 10^{22} \text{ cm}^{-2}$ and unabsorbed for those with columns below this value. As justified in Section 7.4, this N_H value represents the amount of absorbing neutral gas needed to hide the broad emission line region (BLR), assuming a Milky Way gas-to-dust ratio and $\alpha_{OX} = 1.48$ for each AGN, in a $5L_*$ host galaxy. As discussed below, most AGN with unabsorbed X-ray emission show signs of optical emission from the BLR. Alternatively, judging by the lack of broad emission lines, most X-ray absorbed AGN have significant optical extinction. However, there is a small though significant fraction that do not fall into the simple obscured or unobscured scenario. The various classes illustrating the permutations of X-ray absorption and optical extinction are delineated in the following sections.

7.1. Unabsorbed AGN with Broad Emission Lines

We find that the majority of AGN with unabsorbed ($N_H < 10^{22} \text{ cm}^{-2}$) X-ray emission have no apparent extinction of their optical light. First, the optical spectra of 80% of the unabsorbed AGN ($HR < -0.2$; Figure 2) are characterized by the presence of broad emission lines (e.g., Ly α , CIV, CIII], MgII). In Figure 9, we plot the X-ray hardness ratio as a function of optical color for our AGN sample. These BLAGN have blue optical colors and are grouped in a region ($HR < -0.4$ and $g'-i' < 1$) characteristic of unobscured AGN. As mentioned previously, our BLAGN sample at $z > 1$ has colors similar to the optically-selected SDSS quasars (Figure 6a) but with a slightly broader and skewed distribution (Figure 7). We conclude that no significant obscuring material is preventing us from observing the broad line region in these unabsorbed AGN.

We find that 10% of ChaMP BLAGN have red optical colors with $g'-i' > 1.0$ (Figure 9), offset from the locus of SDSS quasars (Figure 6a). We suspect that host galaxy emission is contributing to their red optical color since these ChaMP BLAGN, mostly at $z < 1$, represent the lower luminosity fraction of our sample ($L_{2-8\text{keV}} < 10^{44} \text{ erg s}^{-1}$; Figure 3). To further illustrate, Figure 6b shows that the absolute magnitudes ($M_{i'}$) and colors of these red BLAGN are intermediate between the non-BLAGN and the more luminous ($M_{i'}$) AGN. We present in Figure 5, optical spectra of two such objects with composite (AGN+host) spectra. Both of these AGN have broad optical emission lines but their red optical continuum is dominated by the host galaxy. Extinction due to dust might contribute to both their low luminosity and optical color. Dust extinction is probably responsible for the red colors of three luminous ($L_{2-8\text{keV}} > 10^{44} \text{ erg s}^{-1}$) BLAGN seen in Figure 6a with $1.5 < z < 2.0$. The ChaMP BLAGN might be a fainter version of the 2MASS selected, red and X-ray unabsorbed BLAGNs (Wilkes et al. 2002).

7.2. Unabsorbed AGN Lacking Broad Emission Lines

Surprisingly, a number of unabsorbed AGN show no broad optical emission lines. These objects are clearly seen in Figure 9 with $HR < -0.2$ and $g'-i' > 1.0$. The nature of these sources is the least understood. Their red optical colors are characteristic of their host galaxy but the classification might be due to the fact that at certain redshifts, we lose the AGN diagnostic emission lines

(e.g. H α , Mg II) within the observed optical spectroscopic window for sources with comparable host galaxy and AGN optical emission as discussed in Section 6.3. Usually H β is the only line available, which can suffer from both extinction and contamination due to the host galaxy. We are pursuing spectroscopy further to the red for some of these objects to detect H α for emission line diagnostics to securely identify the ionizing source as either an AGN or starburst. Many of these AGN are at $z > 0.4$ with H α at $\lambda > 9200$ Å, making this type of analysis difficult for optically faint AGN.

Two bright NELG may provide insight into the nature of this class of unabsorbed AGN ($N_{\text{H}} < 10^{22}$ cm $^{-2}$). These objects might be similar to the rare unabsorbed Seyfert 2 galaxies seen by other groups in nearby objects (Georgantopoulos & Zezas 2003; Panessa & Bassani 2002). With over 400 counts in both sources [CXOMP J054319.2-405750 (#50; $\log L_{\text{X}} = 43.05$; $M_{\text{V}} = -22.05$), CXOMP J214001.4-234112 (#159; $\log L_{\text{X}} = 43.08$; $M_{\text{V}} = -22.35$)], we are able to constrain their X-ray spectral properties. We fit the data using a spectral model with the photon index and the intrinsic absorption as free parameters (see Section 3.1). Figure 10 shows the X-ray and optical spectra. Source #50 is very soft with $\Gamma = 2.29_{-0.16}^{+0.22}$ and $N_{\text{H}} < 8.2 \times 10^{20}$ cm $^{-2}$. There could possibly be a soft excess below 2 keV. Source #159 has a photon index $\Gamma = 1.83_{-0.13}^{+0.21}$ with $N_{\text{H}} < 7.6 \times 10^{20}$ cm $^{-2}$. These AGN show no signs of X-ray absorption while their optical spectra show a strong galaxy continuum with overlying narrow emission lines. The width of H β is 323 km s $^{-1}$ in source #50 and the width of H α is 669 km s $^{-1}$ in #159. Surprisingly, their low ionization emission line ratios are not typical of an AGN, but resemble those of a star forming galaxy. We can explain the X-ray and optical properties with any of the following scenarios: (1) severe dilution of the AGN emission by a host undergoing prodigious star formation, (2) a Compton thick obscuring medium in which we observe the indirect, reflected component of the X-ray emission and the optical light is purely from the host galaxy due to severe dust extinction, (3) a high dust to neutral gas ratio which allows only the X-rays to penetrate or (4) beamed emission from a BL Lac. To properly discriminate between these models, a sample of nearby AGN for which we can resolve the nuclear region and properly subtract the host emission would be ideal. For the Compton thick case, the true L_{X} may be much higher. In addition, we may find a large L_{IR} from reprocessed emission.

We are finding a population of optically ‘dull’ galaxies (Severgnini et al. 2003; Silverman et al. 1998; Tananbaum et al. 1997; Elvis et al. 1981), recently coined XBONGS (Comastri et al. 2002). These are galaxies with X-ray bright nuclei that have weak or nonexistent emission lines. All but a couple of the 13 ALG identified in this study are not heavily absorbed (Figure 9). Similar X-ray properties have been noted in recent studies of other examples (e.g., Severgnini et al. 2003). As shown in Figure 5, we may be able to detect AGN optical signatures in some of these ALG using expanded wavelength coverage to include H α , which is less susceptible to dust extinction and stellar absorption features. Using the definition of Dressler & Shechtman (1987), only two

are possible BL Lac candidates based upon their 4000 Å break contrast.

7.3. Absorbed AGN

We find that most X-ray absorbed ($N_{\text{H}} > 10^{22}$ cm $^{-2}$) AGN suffer from optical extinction. Almost all of the AGN (84%) with $\text{HR} > -0.2$, lack broad optical emission lines (Figure 9). These absorbed AGN tend to have narrow emission lines in their optical spectra. At these redshifts ($z > 0.4$), the optical spectra rarely include a detection of all the emission lines (H α , NII, [OIII], H β) needed to solidify the optical classification as an AGN as opposed to a star forming galaxy. Given their high X-ray luminosity ($L_{\text{X}} > 10^{42}$ erg s $^{-1}$), we are confident that the X-ray emission is due to supermassive black hole accretion.

In Figure 9, we show that these absorbed AGN ($\text{HR} > -0.2$) have red optical colors ($g'-i' > 1.5$) characteristic of their host galaxy and not the AGN itself (Green et al. 2004; Fiore et al. 2003). Most of these AGN have colors offset from the locus of optically-selected QSOs and fall along the track of an early type galaxy as shown in Figure 6a. These results agree with studies which conclude that AGN are predominantly found in massive, early type galaxies (Kauffmann et al. 2003). For the most part, AGN which suffer from absorption in the X-rays have significant optical extinction that hides emission from the BLR.

7.4. Intrinsic N_{H}

We have measured the amount of intrinsic absorption towards each AGN by fitting the X-ray count distribution with a fixed powerlaw model as described in Section 3.1. In Figure 11, we plot the best fit intrinsic N_{H} as a function of rest frame X-ray luminosity. Measurements with errors (1.6σ) are plotted as filled symbols. Upper limits are marked as hollow symbols placed at the 1.6σ upper limit with a downward arrow.

The absorbed AGN have columns in the range of $10^{22} < N_{\text{H}} < 10^{24}$ cm $^{-2}$. The majority of these are optically classified as NELG. We have uncovered 5 luminous AGN with $L_{2-8\text{keV}} > 10^{44}$ erg s $^{-1}$ which are heavily absorbed with well-constrained columns ($N_{\text{H}} > 10^{22}$ cm $^{-2}$). These quasars would not be singled out as having high absorption based on their hardness ratios since they are mostly at $z > 1.7$, where the observed X-ray counts are less affected by absorption. (In Figure 9, the BLAGN with well constrained values of N_{H} (filled symbols) do not necessarily have $\text{HR} > -0.2$.) While these quasars have broad emission lines in their optical spectra (Figure 12), they all show signs of either absorption or extinction in the optical. Two sources (12a,d) have a reddened optical continuum possibly attributed to dust extinction and similar to the red quasar 3C 212 (Elvis et al. 1994). Their colors are substantially offset from the SDSS quasar locus in Figure 6. Three (12b,c,d) have narrow absorption lines that might be related to the X-ray absorption. Source CXOMP J230240.2+083611 (#176 in 12b) has an absorption line blue-shifted from the emission line center. This is evidence for ionized intrinsic outflows which are known to have high absorbing gas columns ($N_{\text{H}} \sim 6 \times 10^{22}$ cm $^{-2}$) in BALQSOs (Green et al. 2001). Even in non-BALQSOs, (Laor & Brandt 2002) found

an association in quasars between (soft) X-ray weakness and CIV absorption equivalent width. While the spectrum of source CXOMP J230211.1+084657 (#173, Figure 12e) has a poor S/N ratio, absorption might be seen blueward of the CIV emission line. The object CXOMP J134450.6+555531 (#113 in 12c) has narrow absorption lines detached from the emission lines. Either these absorption lines are extremely fast outflows intrinsic to the AGN or a more probable explanation is an intervening absorber. Based on these 5 absorbed quasars, we find that 6% (5/79) of luminous ($L_{2-8\text{keV}} > 10^{44}$ erg s^{-1}) X-ray-selected BLAGN have $N_{\text{H}} > 10^{22}$ cm^{-2} (2% of all AGNs). This is consistent with the value of 10% found by Perola et al. (2004) and Page et al. (2003).

As expected, the unabsorbed ($N_{\text{H}} < 10^{22}$ cm^{-2} ; Figure 11) AGN population is dominated by BLAGN. Almost all of the measurements are poorly constrained (upper limits) with a low probability of significant absorption. The apparent trend of increasing N_{H} with luminosity for the BLAGN is probably due to our decreasing sensitivity to the absorbing column at higher redshifts, rest frame soft X-rays, most susceptible to absorption, are redshifted out of the *Chandra* bandpass. There are a fair number of NELG and ALG with no measurable absorbing column. As described in the previous section, we suspect that host dilution is confusing the spectroscopic characterization of these sources.

We crudely estimate the N_{H} needed to hide the optical emission from an embedded AGN of a given X-ray luminosity. From the rest frame $L_{2.0-8.0\text{keV}}$ and $\alpha_{\text{OX}}=1.48$ (the mean X-ray to optical flux ratio for the X-ray selected BLAGN; Section 6.3), we calculate the expected unabsorbed l_{ν} (2500 Å). We then compare the 2500 Å monochromatic luminosity to that of a host galaxy, assuming $L_{\text{Host}} = 5L_{\star}$. This luminosity corresponds to the average host absolute magnitude ($M_B = -23.0$) found by Jahnke & Wisotzki (2003) for a sample of bright QSOs. Using the gas-to-dust ratio of the Milky Way ($N_{\text{H}} = 4.82 \times 10^{21}$ $E_{\text{B-V}}$ mag^{-1} cm^{-2}) and Small Magellanic Cloud ($N_{\text{H}} = 4.52 \times 10^{22}$ $E_{\text{B-V}}$ mag^{-1} cm^{-2}) from Pei (1992), we determine the amount of dust extinction and hence the column density required to diminish the AGN optical light to a tenth of the assumed host optical luminosity. The dashed lines in Figure 11 shows the results from this rather simplified calculation for both gas-to-dust ratios. Based on the gas-to-dust ratio of the Milky Way, the column densities needed to hide an AGN are $N_{\text{H}} \sim 10^{22}$ cm^{-2} which marks our division between absorbed and unabsorbed AGN. The column densities could potentially be higher (Fig 11; top, dashed line), given that luminous quasars found in the SDSS have dust extinction more typical of the Small Magellanic Cloud (Hopkins et al. 2004).

7.5. Optically faint X-ray sources and type 2 quasars

As evident from Figure 1, there are many unidentified X-ray sources with $r' > 22$. We believe that a significant fraction of these sources may be the elusive type 2 quasars.

A number of ongoing X-ray surveys (e.g., CDF-N and CDF-S) have acquired spectroscopic redshifts fainter than the current ChaMP sample and have identified a few as luminous narrow line AGN. The HELLAS2XMM (Fiore et al. 2003) survey has spectroscopically identi-

fied 8 type 2 QSOs from a sample of 13 over 0.9 deg^2 with $f_X/f_{r'} > 10$. The redshift range of these quasars ($0.7 < z < 1.8$) as described previously has been inaccessible to ChaMP (Figure 3) due to our bright spectroscopic limit.

To investigate the lack of obscured, highly luminous quasars in our sample, we illustrate their expected location in f_X-r' space (Figure 13). We plot only the X-ray bright ($f_{2-8\text{keV}} > 1 \times 10^{-14}$ erg cm^{-2} s^{-1}) extragalactic sources (with the exclusion of clusters) and the unidentified objects. We have shaded the region for a hypothetical quasar with $L_X = 10^{44}$ erg s^{-1} and optical emission purely from a host elliptical galaxy ($L_{\star} < L_r < 10L_{\star}$) using HyperZ (Bolzonella, Miralles, & Pell 2000). We have labelled the redshifts ($0.05 < z < 1.0$) in this region with dashed vertical lines. We infer that most obscured quasars probably fall within the region with $r' > 22$ based on our X-ray sensitivity and area coverage.

To test this hypothesis, we have included data from the CDF-N and CDF-S which have detected 6 type 2 quasars with $f_x > 1 \times 10^{-14}$ erg cm^{-2} s^{-1} , $L_{2-8\text{keV}} > 10^{44}$ erg s^{-1} and no evidence for any broad optical emission lines. The optical magnitudes of these sources have been converted to the SDSS photometric system using the transformations in Fukugita (1996). For the CDF-S data, we use average colors for each object class from the CDF-N sources to convert the R band magnitude (Szokoly et al. 2003). It is apparent from the six possible type 2 quasars in the deep fields that there is potentially a significant number of obscured quasars yet to be identified at faint optical magnitudes.

The optically undetected, X-ray bright objects must await infrared followup to learn more about their source properties. However, we can look at the X-ray hardness ratios to infer their host optical properties. From Figure 2, we see that the optically undetected sources have a wide range of hardness ratio with many extreme cases ($\text{HR} > 0$). Since these X-ray sources have a HR distribution most similar to the NELG at $f_x > 1 \times 10^{-14}$ erg cm^{-2} s^{-1} , it seems likely that many of these optically undetected sources are the narrow emission line objects at higher redshift possibly comprising a significant fraction of the highly luminous and obscured quasar population.

8. CONCLUSIONS

We have presented an analysis of the X-ray and optical properties of 188 hard X-ray selected AGN in 20 medium depth ChaMP fields. These AGN have been classified by optical spectroscopy to be comprised of BLAGN (69%), NELG (24%) or ALG (7%). Overall, we find that 81% of the AGN agree with simple AGN unification models (Antonucci 1993). The two main points of evidence are as follows:

- 80% of unabsorbed AGN ($N_{\text{H}} < 10^{22}$ cm^{-2}) have optical properties characterized by broad emission lines. The optical colors of ChaMP BLAGN are predominately blue ($g' - i' < 1.0$) and similar to optically-selected quasars from the SDSS but with a slightly wider distribution. A significant red ($g' - i' > 1.0$) BLAGN population exists with optical properties influenced by their host galaxy. These objects represent 10% of the full AGN sample.
- 84% of absorbed AGN ($N_{\text{H}} > 10^{22}$ cm^{-2}) lack

broad optical emission lines. Most are associated with NELG with column densities in the range $10^{22} < N_{\text{H}} < 10^{24} \text{ cm}^{-2}$. Their optical colors ($g' - i' > 1.0$) are characteristic of a luminous, early type galaxy.

We also find a number of atypical AGN (19%) whose X-ray and optical properties can be explained without any need to alter the AGN unification models.

- The lack of broad optical emission lines in X-ray unabsorbed, NELG and ALG can be attributed to a strong host galaxy contribution in 17% of the total AGN sample.
- The large amount of X-ray absorption ($N_{\text{H}} > 10^{22} \text{ cm}^{-2}$) in a few BLAGN (2% of all AGNs) may be related to signatures of absorption in their optical spectra. A future ChaMP study will determine if the X-ray absorption is associated with warm (ionized) intrinsic outflowing gas similar to that seen in Broad Absorption Line quasars.

We are greatly indebted to NOAO and the SAO TAC for their support of this work. Many thanks to Robert Kirshner, Warren Brown, John Huchra, Kevin Krisciunas, and Guillermo Torres for contributing to the ChaMP spectroscopic program. We remain indebted to the staffs at Kitt Peak, CTIO, Las Campanas, Keck, FLWO, and MMT for assistance with optical observations.

We gratefully acknowledge support for this project under NASA under CXC archival research grants AR3-4018X and AR4-5017X. TLA, WAB, RAC, PJG, DWK, AEM, HT, and BW also acknowledge support through NASA Contract NASA contract NAS8-39073 (CXC). DW receives support through the SAO Research Experiences for Undergraduates (REU) Summer Intern Program that is supported by the NSF.

REFERENCES

- Akylas, A., Georgantopoulos, I., & Barcons, X. 2003, *A&A*, 403, 869
- Antonucci, R.R.J., & Miller, J.S. 1985, *ApJ*, 297, 621
- Antonucci, R.R.J. 1993, *ARA&A*, 31, 473
- Barcons, X., Carrera, F. J., Ceballos, M.T., Mateos, S., Page, M.J., Prez-Fournon, I., & Watson, M.G., The XMM-Newton Survey Science Centre 2003, *AN*, 324, 44
- Barger, A.J., Cowie, L.L., Brandt, W.N., Capak, P., Garmire, G.P., Hornschemeier, A.E., Steffen, A.T., & Wehner, E.H. 2002, *AJ*, 124, 1839
- Barger, A.J., Cowie, L.L., Capak, P., Alexander, D.M., Bauer, F.E., Fernandez, E., Brandt, W.N., & Garmire, G.P. *AJ*, 126, 632
- Bertin, E., & Arnouts, S. 1996 *A&AS* 117, 393
- Bolzonella, M., Miralles, J.-M., & Pell, R. 2000, *A&A* 363, 476
- Comastri, A., Setti, G., Zamorani, G., & Hasinger, G. 1995, *A&A*, 296, 1
- Comastri, A. et al. 2002, *ApJ*, 571, 771
- Cowie, L.L., Garmire, G.P., Bautz, M.W., Barger, A.J., Brandt, W.N., & Hornschemeier, A.E. 2002, *ApJ*, 566, L5
- Cowie, L.L., Barger, A.J., Bautz, M.W., Brandt, W.N., & Garmire, G.P. 2003 *ApJ*, 584, L57
- Dickey, J.M., & Lockman, F.J. 1990, *ARA&A*, 28, 215
- Dressler, A., & Shechtman, S. 1987, *AJ*, 94, 899
- Elvis, M., Schreier, E.J., Tonry, J., Davis, M., & Huchra, J.P. 1981, *ApJ*, 246, 20
- Elvis, M., Fabrizio, F., Mathur, S., & Wilkes, B.J. 1994, *ApJ*, 425, 103
- Fiore, F. et al. 2003, *A&A*, 409, 79
- Fukugita, M., Ichikawa, T., Gunn, J.E., Doi, M., Shimasaku, K., & Schneider, D.P. 1996, *AJ*, 111, 1748
- Georgantopoulos, I., & Zezas, A. 2003, *ApJ*, 594, 704
- Gilli, R., Salvati, M., & Hasinger, G. 2001, *A&A*, 366, 407
- Green, P.J., Aldcroft, T.L., Mathur, S., Wilkes, B., & Elvis, M. 2001, *ApJ*, 558, 109
- Green et al. 2004, *ApJS*, 150, 43
- Hasinger, G., Burg, R., Giacconi, R., Schmidt, M., Trumper, J., & Zamorani, G. 1998, *A&A*, 329, 482
- Hasinger, G. et al. 2001, *A&A*, 365, 45
- Harrison, F.A., Eckart, M.E., Mao, P. H., Helfand, D.J., & Stern, D. 2003, *ApJ*, 596, 944
- Ho, L.C., Filippenko, A.V., Sargent, W.L., Peng, C.Y. 1997, *ApJS*, 112, 391
- Hopkins, P.F. et al. 2004, astro-ph/0406293
- Jahnke, K., & Wisotzki, L. 2003, *MNRAS*, 346, 304
- Kauffmann, G. et al. 2003, *MNRAS*, 346, 1055
- Kim, D.-W. et al. 2004a, *ApJS*, 150, 19
- Kim, D.-W. et al. 2004b, *AJ*, 600, 59
- Laor, A., & Brandt, W. N. 2002, *ApJ*, 569, L641
- Lira, P., Ward, M., Zezas, A., Alonso-Herrero, A., & Ueno, S. 2002, *MNRAS*, 330, 259
- Mainieri, V., Bergeron, J., Hasinger, G., Lehmann, I., Rosati, P., Schmidt, M., Szokoly, G., & Della Ceca, R. 2002, *A&A*, 393, 425
- Moran, E.C., Filippenko, A.V., & Chornock, R. 2002, *AJ*, 579, L71
- Moretti, A., Campana, S., Lazzati, D., & Tagliaferri, G. 2003, *ApJ*, 588, 696
- Mukai, K. 1993, *HEASARC Newsletter*, (Legacy) 3, 21
- Mushotzky, R.F., Cowie, L.L., Barger, A.J., & Arnaud, K.A. 2000, *Nature*, 404, 459
- O'Sullivan, E., Forbes, D.A., & Ponman, T.J. 2001, *MNRAS*, 328, 461
- Page, M.J. et al. 2003, *AN*, 324, 101
- Panessa, F., & Bassani, L. 2002, *A&A*, 394, 435
- Pei, Y.C. 1992, *ApJ*, 395, 130
- Perola, G.C. et al. 2004, astro-ph/0404044
- Piconcelli, E., Cappi, M., Bassani, L., Di Cocco, G., & Dadina, M. 2003, *A&A*, 412, 689
- Reeves, J.N., & Turner, M.J.L. 2000, *MNRAS*, 316, 234
- Richards, G.T. et al. 2001, *AJ*, 121, 2308
- Schlegel, E. M., & Salinas, A. 2004, in *Magnetic Cataclysmic Variables*, ed. M. Cropper & S. Vrieland, (San Francisco: ASP Conference Series), in press
- Schneider, D.P. et al. 2003, *AJ*, 126, 2579
- Severgnini, P. et al. 2003, *A&A*, 406, 483
- Silverman, J.D., Harris, D.E., & Junor, W. 1998, *A&A*, 335, 443
- Smith, D.A., & Done, C. 1996, *MNRAS*, 280, 355
- Stocke, J.T., Morris, S.L., Gioia, I.M., Maccacaro, T., Schild, R., Wolter, A., Fleming, T.A., & Henry, J.P. 1991, *ApJS*, 76, 813
- Szokoly, G.P. et al. 2003, astro-ph/0312324
- Tananbaum, H., Tucker, W., Prestwich, A., & Remillard, R. 1997, *ApJ*, 476, 83
- Tozzi, P. et al. 2001, *ApJ*, 562, 42
- Turner, T.J., George, I.M., Nandra, K., & Mushotzky, R.F. 1997, *ApJ*, 488, 164
- Valdes, F. G. 2002, in *Automated Data Analysis in Astronomy*, eds Ranjan Gupta, Harinder P. Singh, and Coryn A. L. Bailer-Jones, Narosa Publishing House, New Delhi, p. 309.
- Wilkes, B.J., Schmidt, G.D., Cutri, R.M., Ghosh, H., Hines, D., Nelson, B., & Smith, P.S. 2002, *ApJ*, 564, L65
- Yuan, W., Brinkmann, W., Siebert, J., & Voges, W. 1998, *A&A*, 330, 108
- Zakamska, N.L. et al. 2003, *AJ*, 126, 2125
- Zezas, A., Ward, M.J., & Murray, S.S. 2003, 594, 31

TABLE 1
Chandra FIELDS

ObsID	PI Target	Exposure ^a (ksec)	ACIS CCDs ^b	RA	DEC J2000 ^c	UT Date	Galactic N _H ^d (10 ²⁰ cm ⁻²)
520	MS0015.9+1609	61.0	<u>0123</u>	00:18:33.4	+16:26:34.8	2000 Aug 18	4.06
913	CLJ0152.7-1357	34.6	<u>0123</u> 67	01:52:43.0	-13:57:30.0	2000 Sep 08	1.61
796	SBS 0335-052	47.0	<u>0123</u>	03:37:44.0	-05:02:39.0	2000 Sep 07	4.98
624	LP944-20	40.9	<u>2367</u>	03:39:34.7	-35:25:50.0	1999 Dec 15	1.44
902	MS0451.6-0305	41.5	<u>2367</u>	04:54:10.9	-03:01:07.2	2000 Oct 08	5.18
914	CLJ0542-4100	48.7	<u>0123</u>	05:42:50.2	-41:00:06.9	2000 Jul 26	3.59
1602	Q0615+820	43.1	<u>2367</u>	06:26:02.9	+82:02:25.5	2001 Oct 18	5.27
377	B2 0738+313	26.9	<u>367</u>	07:41:10.7	+31:12:00.4	2000 Oct 10	4.18
2130	3C207	30.0	<u>2367</u>	08:40:48.0	+13:12:23.0	2000 Nov 04	4.14
512	EMSS1054.5-0321	75.6	<u>2367</u>	10:57:00	-03:37:00.0	2000 Apr 21	3.67
536	MS1137.5+6625	114.6	<u>0123</u>	11:40:23.3	+66:08:42.0	1999 Sep 30	1.18
809	MRK 273X	40.9	<u>2367</u>	13:44:47.5	+55:54:10.0	2000 Apr 19	1.09
541	V1416+4446	29.8	<u>0123</u>	14:16:28.8	+44:46:40.8	1999 Dec 02	1.24
548	RXJ1716.9+6708	50.3	<u>0123</u>	17:16:52.3	+67:08:31.2	2000 Feb 27	3.71
830	Jet of 3C390.3	23.6	<u>2367</u>	18:41:48.1	+79:47:43.0	2000 Apr 17	4.16
551	MS2053.7-0449	42.3	<u>0123</u> 6	20:56:22.2	-04:37:44.4	2000 May 13	4.96
928	MS2137-2340	29.1	<u>2367</u>	21:40:12.7	-23:39:27.0	1999 Nov 18	3.57
431	Einstein Cross	21.9	<u>2367</u>	22:40:30.4	+03:21:31.0	2000 Sep 06	5.34
918	CLJ2302.8+0844	106.1	<u>0123</u>	23:02:48.1	+08:44:00.0	2000 Aug 05	5.50
861	Q2345+007	65.0	<u>267</u>	23:48:19.6	+00:57:21.1	2000 Jun 27	3.81

^aEffective screened exposure time for the on-axis chip.

^bThe ACIS CCD chips used in the observation with the aimpoint chip underlined. CCD 8 has been excluded (see text).

^cNominal target position, not including any *Chandra* pointing offsets.

^dGalactic column density taken from Dickey & Lockman (1990).

TABLE 2
 KPNO 4M OPTICAL IMAGING ^a

ObsID	UT Date	Filter	Dithers	Exposure (total sec)	Airmass (Mean)	FWHM ^b (")	m _{TO} ^c Limit	m _{5σ} ^d Limit
377	21 Feb 2001	<i>g'</i>	3	1800	1.00	1.1	25.4	26.5
		<i>r'</i>	3	1500	1.01	1.0	24.9	26.0
		<i>i'</i>	3	1500	1.04	1.1	24.1	25.2
431	11 Jun 2000	<i>g'</i>	2	1000	1.36	1.6	24.1	25.4
		<i>r'</i>	1	500	1.28	1.6	23.4	24.7
		<i>i'</i>	1	360	1.25	1.2	22.9	24.1
512	21-22 Feb 2001	<i>g'</i>	5	4500	1.29	1.3	24.9	26.3
		<i>r'</i>	3	2400	1.23	1.1	24.4	25.8
		<i>i'</i>	5	2000	1.29	1.3	23.6	24.8
520	25 Oct 2001	<i>g'</i>	3	1950	1.24	1.2	24.1	25.2
		<i>r'</i>	3	1200	1.34	1.2	23.9	24.9
		<i>i'</i>	3	900	1.46	1.4	22.6	24.0
548	10 Jun 2000	<i>g'</i>	2	1800	1.28	1.2	24.8	26.2
		<i>r'</i>	2	1200	1.24	1.3	24.1	25.4
		<i>i'</i>	2	1200	1.22	1.7	23.4	24.6
551	10,12 Jun 2000	<i>g'</i>	3	2100	1.28	1.7	24.4	25.6
		<i>r'</i>	4	1200	1.25	1.8	23.9	25.0
		<i>i'</i>	2	600	1.24	1.4	22.9	24.5
796	24 Oct 2001	<i>g'</i>	3	2700	1.33	1.1	25.1	26.4
		<i>r'</i>	3	2400	1.52	1.2	24.6	25.7
		<i>i'</i>	3	1200	1.28	1.1	23.6	24.8
809	11 June 2000	<i>g'</i>	3	2100	1.19	1.8	23.1	24.4
		<i>r'</i>	3	1500	1.14	1.7	23.4	24.6
		<i>i'</i>	3	1500	1.10	1.8	23.1	24.4
830	11 June 2000	<i>g'</i>	3	1800	1.49	1.6	24.1	25.6
		<i>r'</i>	2	1000	1.49	1.6	23.4	24.8
		<i>i'</i>	1	600	1.49	1.6	22.9	24.2
902	23 Oct 201	<i>g'</i>	3	1800	1.24	1.0	24.9	26.2
		<i>r'</i>	3	1800	1.22	1.1	24.4	25.6
		<i>i'</i>	3	1200	1.24	1.0	23.6	24.9
913	23 Oct 2001	<i>g'</i>	5	3500	1.46	1.1	25.1	26.4
		<i>r'</i>	5	3000	1.44	1.0	24.6	25.9
		<i>i'</i>	5	2000	1.52	1.1	23.6	24.8
918	23 Oct 2001	<i>g'</i>	5	4500	1.20	1.2	24.9	26.0
		<i>r'</i>	5	3000	1.09	1.3	24.1	25.6
		<i>i'</i>	5	1500	1.12	1.2	23.1	24.8
1602	14 Dec 2001	<i>g'</i>	1	520	1.56	2.4	23.3	24.8
		<i>r'</i>	3	1800	1.56	2.1	23.1	24.8
		<i>i'</i>	3	1800	1.56	2.5	22.6	24.7
2130	22 Feb 2001	<i>g'</i>	3	3000	1.16	1.4	25.1	26.5
		<i>r'</i>	3	2700	1.08	1.3	24.9	25.9
		<i>i'</i>	5	2500	1.06	0.9	24.6	25.8

^aWe tabulated 14 additional ChaMP fields following Green et al. (2004).

^bFWHM of point sources in final stacked images.

^cTurnover magnitude limit at $\sim 90\%$ completeness, using 0.25 mag bins before extinction correction, as described in the text.

^dMagnitude limit for a $\sim 5\sigma$ detection.

TABLE 3
OPTICAL SPECTROSCOPIC FOLLOWUP

Telescope	Instrument	Grating/Grism	λ range (\AA)	R ($\lambda/\Delta\lambda$)	Spectral Resolution (\AA)	Number of spectra
WIYN ¹	HYDRA	316@7.0	4500-9000	950	7.8	91
CTIO/4m	HYDRA	KPGL3	4600-7400	1300	4.6	48
Magellan	LDSS-2	med red & blue	3600-8500 ²	520	13.5	41
Magellan	B&C	300 l/mm	3700-8700	384	13.0	7
MMT	Blue Channel	300 l/mm	3500-8300	800	8.8	15
Keck I	LRIS	300/5000	4000-9000	484	13	5
FLWO 1.5m	FAST	300 l/mm	3600-7500	850	5.9	2

¹The WIYN Observatory is a joint facility of the University of Wisconsin Madison, Indiana University, Yale University, and the National Optical Astronomy Observatory.

²Spectral coverage can vary as a function of slit position in the mask.

TABLE 4
X-RAY SOURCE POPULATIONS

Class	All ^a	$r' < 22.5$	$r' < 22.5$ $L_x > 10^{42} \text{ erg s}^{-1}$
BLAGN	139	132	130
NELG	53	52	45
ALG	18	16	13
STAR	10	10	...
Cluster	5	5	...
No z ^b	195	63	...
No opt ^c	82
Total	497 ^d	273	188

^a $f_{2.0-8.0\text{keV}} > 2.7 \times 10^{-15} \text{ erg cm}^{-2} \text{ s}^{-1}$

^bOptical counter-parts with no identification

^cNo optical counter-part in either g' , r' , or i' .

^dNot including clusters are counted under BLAGN, NELG or ALG.

TABLE 5
HARD AGN^a

Src #	ChaMP Name	RA (J2000)	Dec (J2000)	Hard ^b counts	log f _x ^c	HR	z	log L _x ^d	r'	g'-i'	r'-i'	Class	log N _H (cm ⁻²)
1	CXOMP J001845.7+163346	00:18:45.74	+16:33:46.6	89.0±10.7	-13.51	-0.40	0.624	43.70	21.41	1.58	0.66	NELG	21.89 ^{+0.15} _{-0.18}
2	CXOMP J001837.3+163447	00:18:37.38	+16:34:47.1	18.4± 5.8	-14.17	-0.71	2.149	44.37	19.94	0.23	0.15	BLAGN	<21.61
3	CXOMP J001833.4+163154	00:18:33.47	+16:31:54.4	38.0± 7.3	-13.90	-0.65	1.643	44.36	21.11	0.73	0.39	BLAGN	<21.58
4	CXOMP J001837.4+163757	00:18:37.48	+16:37:57.7	19.5± 7.3	-14.13	-0.71	1.506	44.03	20.90	0.45	0.16	BLAGN	<22.35
5	CXOMP J001828.6+163418	00:18:28.68	+16:34:18.2	9.0± 4.4	-14.48	-0.66	1.163	43.40	20.90	0.38	0.04	BLAGN	<21.97
6	CXOMP J001842.0+163425	00:18:42.09	+16:34:25.0	9.3± 4.6	-14.50	>0.04	0.550	42.59	21.23	2.66	0.82	ALG	<22.14
7	CXOMP J001825.0+163653	00:18:25.01	+16:36:53.0	15.6± 6.1	-14.25	-0.49	1.198	43.67	21.56	<-2.07	<-2.47	BLAGN	<22.28
8	CXOMP J001850.1+162756	00:18:50.14	+16:27:56.4	20.5± 5.9	-14.16	-0.63	1.330	43.87	21.21	0.35	-0.06	BLAGN	<22.06
9	CXOMP J001859.8+162649	00:18:59.83	+16:26:49.3	67.0±10.0	-13.63	-0.64	1.714	44.67	19.92	0.31	0.27	BLAGN	<22.15
10	CXOMP J001854.9+162952	00:18:54.92	+16:29:52.8	10.1± 4.9	-14.46	-0.68	2.950	44.41	21.78	0.21	-0.14	BLAGN	<22.54
11	CXOMP J001810.2+163223	00:18:10.24	+16:32:23.9	54.2± 8.8	-13.72	-0.61	1.273	44.26	19.62	0.33	0.01	BLAGN	<21.46
12	CXOMP J001801.7+163426	00:18:01.72	+16:34:26.0	42.6± 9.3	-13.81	-0.09	0.329	42.74	19.76	1.63	0.34	NELG	22.33 ^{+0.20} _{-0.21}
13	CXOMP J001827.0+162900	00:18:27.08	+16:29:00.1	13.1± 4.8	-14.33	-0.55	2.828	44.49	21.27	0.10	-0.16	BLAGN	<23.02
14	CXOMP J015327.3-135223	01:53:27.30	-13:52:23.8	123.7±13.3	-13.02	-0.65	0.326	43.52	19.01	0.88	0.19	BLAGN	<21.13
15	CXOMP J015311.1-135104	01:53:11.14	-13:51:04.3	64.9± 9.7	-13.36	-0.44	0.949	44.30	21.37	0.32	0.19	BLAGN	<21.71
16	CXOMP J015312.3-135723	01:53:12.39	-13:57:23.5	27.2± 6.7	-13.76	-0.61	1.454	44.36	20.45	0.57	0.14	BLAGN	<21.87
17	CXOMP J015308.0-135801	01:53:08.06	-13:58:01.0	13.1± 5.0	-14.05	-0.74	1.793	44.29	19.37	0.23	0.21	BLAGN	<21.68
18	CXOMP J015234.7-134735	01:52:34.70	-13:47:35.8	23.9± 7.9	-13.77	>0.25	0.168	42.12	17.84	0.93	0.36	BLAGN	21.88 ^{+0.74} _{-0.26}
19	CXOMP J015243.8-135900	01:52:43.83	-13:59:00.7	42.7± 7.6	-13.57	-0.72	1.674	44.71	20.88	0.12	0.08	BLAGN	<21.14
20	CXOMP J015239.8-135740	01:52:39.88	-13:57:40.3	75.9± 9.8	-13.31	-0.31	0.868	44.25	21.47	1.71	0.68	BLAGN	22.31 ^{+0.13} _{-0.14}
21	CXOMP J015234.8-140205	01:52:34.87	-14:02:05.3	14.0± 5.5	-14.02	-0.68	1.812	44.34	22.08	0.67	0.45	BLAGN	<21.99
22	CXOMP J015234.7-135929	01:52:34.76	-13:59:29.1	9.8± 4.4	-14.19	-0.54	0.744	43.21	20.69	0.81	0.43	BLAGN	<21.94
23	CXOMP J015235.4-140336	01:52:35.45	-14:03:36.2	14.2± 6.2	-14.01	-0.36	2.418	44.66	21.98	0.30	0.07	BLAGN	<22.76
24	CXOMP J033752.4-045549	03:37:52.44	-04:55:49.0	57.2± 9.1	-13.54	-0.36	0.371	43.14	19.88	1.52	0.56	NELG	21.70 ^{+0.27} _{-0.38}
25	CXOMP J033812.3-050252	03:38:12.39	-05:02:52.3	13.7± 6.0	-14.16	-0.63	1.464	43.97	21.76	0.60	0.39	BLAGN	<22.05
26	CXOMP J033804.2-050312	03:38:04.20	-05:03:12.5	32.4± 7.0	-13.79	-0.62	0.587	43.37	20.62	1.21	0.74	BLAGN	<21.17
27	CXOMP J033800.4-050811	03:38:00.43	-05:08:11.4	19.9± 6.5	-14.01	-0.55	0.434	42.82	21.09	1.65	0.71	ALG	<20.99
28	CXOMP J033723.1-045602	03:37:23.12	-04:56:02.4	23.8± 7.4	-13.86	-0.42	0.944	43.80	21.91	1.41	0.72	BLAGN	<22.30
29	CXOMP J033731.4-050502	03:37:31.44	-05:05:02.2	11.3± 4.7	-14.26	>0.22	0.295	42.19	19.65	1.78	0.64	NELG	23.70 ^{+0.47} _{-0.57}
30	CXOMP J033717.0-050455	03:37:17.05	-05:04:55.4	31.8± 7.8	-13.78	-0.46	1.859	44.60	20.79	0.16	0.46	BLAGN	<22.34
31	CXOMP J034015.4-352848	03:40:15.43	-35:28:48.6	57.6± 9.8	-13.45	-0.79	1.737	44.86	18.80	0.17	0.20	BLAGN	<21.33
32	CXOMP J033940.2-353040	03:39:40.20	-35:30:40.3	16.7± 5.5	-14.04	-0.74	0.454	42.84	21.08	1.38	0.51	NELG	<21.56
33	CXOMP J034019.2-353124	03:40:19.21	-35:31:24.8	29.4± 9.4	-13.69	-0.66	1.348	44.35	21.38	0.39	0.06	BLAGN	<22.28
34	CXOMP J033942.8-352409	03:39:42.89	-35:24:09.6	25.7± 6.3	-13.89	-0.87	1.042	43.87	18.93	0.08	-0.07	BLAGN	<20.74
35	CXOMP J033938.2-352351	03:39:38.23	-35:23:51.9	16.8± 5.3	-14.07	-0.76	0.465	42.84	21.16	0.98	0.38	BLAGN	<21.07
36	CXOMP J033912.1-352811	03:39:12.13	-35:28:11.4	158.5±13.8	-12.78	-0.68	0.463	44.12	20.11	1.75	0.62	BLAGN	<21.54
37	CXOMP J033949.7-352348	03:39:49.77	-35:23:48.8	12.2± 4.8	-14.21	-0.40	0.522	42.82	20.41	2.16	0.66	NELG	<22.05
38	CXOMP J033934.1-352349	03:39:34.19	-35:23:49.3	13.1± 4.8	-14.18	>0.24	0.533	42.87	21.52	2.50	0.95	NELG	23.33 ^{+0.78} _{-0.26}
39	CXOMP J033909.6-352707	03:39:09.67	-35:27:07.3	13.3± 5.9	-14.14	-0.77	0.525	42.89	20.61	1.68	0.61	NELG	<21.51
40	CXOMP J045452.6-025511	04:54:52.68	-02:55:11.8	45.3±10.5	-13.57	>0.47	0.619	43.64	21.16	1.85	0.77	NELG	23.01 ^{+0.16} _{-0.16}
41	CXOMP J045407.1-025400	04:54:07.10	-02:54:00.9	17.8± 5.6	-14.03	-0.61	1.193	43.88	21.48	0.09	-0.41	BLAGN	<21.46
42	CXOMP J045422.1-025124	04:54:22.11	-02:51:24.6	49.8± 9.1	-13.57	-0.65	0.292	42.86	19.03	1.73	0.51	BLAGN	<21.10
43	CXOMP J045415.4-025429	04:54:15.40	-02:54:29.2	10.2± 4.6	-14.29	-0.56	0.491	42.67	21.17	2.22	0.76	ALG	<21.68
44	CXOMP J045424.7-025849	04:54:24.78	-02:58:49.1	22.9± 6.0	-13.94	-0.43	0.724	43.43	20.99	2.36	1.06	NELG	<21.39
45	CXOMP J045422.6-030034	04:54:22.62	-03:00:34.6	12.0± 4.7	-14.23	-0.73	1.936	44.20	20.77	0.28	0.34	BLAGN	<21.49
46	CXOMP J045419.6-030419	04:54:19.66	-03:04:19.9	100.5±11.5	-13.29	-0.75	0.775	44.15	18.29	0.34	0.16	BLAGN	<20.03
47	CXOMP J045356.3-025837	04:53:56.36	-02:58:37.0	95.9±10.9	-13.29	-0.51	0.129	42.35	18.67	1.37	0.44	BLAGN	<20.90
48	CXOMP J045356.7-030225	04:53:56.79	-03:02:25.6	20.2± 6.1	-14.01	>0.50	0.423	42.80	20.05	2.24	0.60	NELG	22.71 ^{+0.38} _{-0.33}
49	CXOMP J054240.8-405626	05:42:40.81	-40:56:26.3	46.5± 7.9	-13.65	+0.69	0.639	43.59	21.06	3.15	1.06	NELG	23.30 ^{+0.13} _{-0.14}
50	CXOMP J054319.2-405750	05:43:19.25	-40:57:50.5	69.4± 9.7	-13.49	-0.71	0.337	43.09	19.33	1.03	0.25	NELG	<20.13

TABLE 5
HARD AGN^a

51	CXOMP	J054328.1-405648	05:43:28.12	-40:56:48.1	13.4± 6.1	-14.17	-0.38	1.185	43.73	21.71	1.04	0.31	BLAGN	<22.29
52	CXOMP	J054330.4-405746	05:43:30.47	-40:57:46.9	38.4± 8.2	-13.73	+0.33	0.423	43.08	21.70	1.86	0.53	NELG	22.83 ^{+0.18} _{-0.19}
53	CXOMP	J054320.6-405619	05:43:20.63	-40:56:19.9	29.0± 7.1	-13.87	+0.10	0.424	42.95	20.71	1.79	0.55	NELG	22.56 ^{+0.15} _{-0.18}
54	CXOMP	J054242.5-405834	05:42:42.51	-40:58:34.0	27.4± 6.4	-13.86	-0.73	1.442	44.25	18.85	0.46	0.08	BLAGN	<21.40
55	CXOMP	J054234.1-405836	05:42:34.11	-40:58:36.7	39.6± 7.4	-13.69	-0.45	0.948	43.97	19.35	0.12	-0.14	BLAGN	22.08 ^{+0.25} _{-0.34}
56	CXOMP	J054225.9-405846	05:42:25.94	-40:58:46.5	33.5± 7.0	-13.77	-0.60	1.462	44.36	20.70	0.67	0.16	BLAGN	<21.83
57	CXOMP	J054232.8-405627	05:42:32.88	-40:56:27.7	18.6± 5.6	-14.03	-0.27	1.191	43.87	22.00	0.75	0.11	BLAGN	<22.66
58	CXOMP	J054255.0-405956	05:42:55.07	-40:59:56.7	32.3± 6.9	-13.84	-0.61	2.628	44.91	20.43	0.22	-0.06	BLAGN	<22.25
59	CXOMP	J054255.0-405922	05:42:55.01	-40:59:22.7	10.4± 4.4	-14.25	>0.28	0.644	43.00	22.25	2.81	0.90	NELG	23.78 ^{+0.36} _{-0.86}
60	CXOMP	J054251.4-410205	05:42:51.46	-41:02:05.2	23.2± 6.0	-13.97	-0.63	0.637	43.27	19.80	1.22	0.60	ALG	<21.70
61	CXOMP	J054248.2-410140	05:42:48.28	-41:01:40.3	18.5± 5.5	-14.07	-0.62	0.634	43.16	20.81	0.60	0.31	NELG	<21.42
62	CXOMP	J054259.5-410241	05:42:59.55	-41:02:41.4	23.1± 6.1	-13.95	-0.27	0.638	43.29	20.67	1.64	0.67	NELG	<22.09
63	CXOMP	J054245.6-410607	05:42:45.62	-41:06:07.0	17.0± 6.3	-14.06	-0.42	0.725	43.32	22.44	1.74	0.82	BLAGN	<21.99
64	CXOMP	J054230.5-410405	05:42:30.58	-41:04:05.0	13.1± 5.6	-14.19	-0.48	1.583	44.02	21.85	1.86	0.70	BLAGN	<22.43
65	CXOMP	J062917.6+820534	06:29:17.66	+82:05:34.2	77.4±10.6	-13.38	-0.58	1.101	44.44	20.76	0.62	0.05	BLAGN	<22.06
66	CXOMP	J063020.5+815938	06:30:20.50	+81:59:38.0	17.6± 8.2	-14.02	-0.81	0.742	43.38	20.31	0.57	0.41	BLAGN	<21.18
67	CXOMP	J062423.8+820938	06:24:23.86	+82:09:38.2	28.9± 7.5	-13.84	-0.63	2.585	44.89	19.60	0.15	0.09	BLAGN	<22.36
68	CXOMP	J062741.2+820406	06:27:41.22	+82:04:06.9	27.3± 6.5	-13.87	-0.64	0.259	42.44	19.47	1.16	0.43	NELG	21.15 ^{+0.32} _{-0.78}
69	CXOMP	J062652.8+820441	06:26:52.81	+82:04:41.2	9.6± 4.4	-14.34	-0.73	2.334	44.29	20.53	0.66	0.40	BLAGN	<21.97
70	CXOMP	J062648.6+815932	06:26:48.64	+81:59:32.6	10.1± 4.6	-14.34	-0.60	2.346	44.30	22.35	0.06	0.16	BLAGN	<22.39
71	CXOMP	J074100.8+311853	07:41:00.81	+31:18:53.0	13.5± 5.2	-13.92	-0.52	0.932	43.72	21.01	0.75	0.11	BLAGN	<22.35
72	CXOMP	J074056.1+311208	07:40:56.14	+31:12:08.6	9.1± 4.3	-14.17	-0.62	0.396	42.57	21.00	1.43	0.39	BLAGN	<21.55
73	CXOMP	J084127.2+131411	08:41:27.21	+13:14:11.5	164.4±14.9	-12.91	-0.75	1.545	45.28	18.93	0.57	0.54	BLAGN	<21.12
74	CXOMP	J084128.2+131106	08:41:28.21	+13:11:06.8	40.9± 9.4	-13.48	-0.66	1.866	44.91	21.04	0.47	0.74	BLAGN	<22.65
75	CXOMP	J084120.2+130721	08:41:20.25	+13:07:21.8	46.9± 9.5	-13.44	-0.61	0.303	43.03	19.13	1.46	0.67	NELG	<21.66
76	CXOMP	J084054.3+131456	08:40:54.30	+13:14:56.6	82.5±10.2	-13.25	-0.69	0.310	43.24	19.65	1.50	0.67	BLAGN	<21.30
77	CXOMP	J084040.8+131726	08:40:40.82	+13:17:26.6	24.5± 6.3	-13.75	-0.60	2.820	45.07	20.33	0.25	0.37	BLAGN	<22.80
78	CXOMP	J084102.9+131716	08:41:02.96	+13:17:16.5	33.0± 7.2	-13.63	>0.48	0.454	43.25	21.17	0.60	0.76	NELG	23.29 ^{+0.23} _{-0.24}
79	CXOMP	J084052.1+131822	08:40:52.12	+13:18:22.9	39.1± 7.6	-13.54	-0.25	0.490	43.42	20.63	2.26	1.03	NELG	22.38 ^{+0.19} _{-0.20}
80	CXOMP	J084045.2+131617	08:40:45.28	+13:16:17.4	13.3± 4.8	-14.04	>0.11	0.573	43.09	21.72	2.36	1.19	NELG	<23.37
81	CXOMP	J084102.5+131313	08:41:02.58	+13:13:13.4	9.2± 4.3	-14.08	-0.70	2.968	44.80	19.28	0.42	0.52	BLAGN	<22.41
82	CXOMP	J105623.1-034315	10:56:23.12	-03:43:15.5	22.7± 9.0	-14.11	-0.37	0.429	42.71	20.94	1.18	0.30	NELG	<22.35
83	CXOMP	J105618.1-034240	10:56:18.10	-03:42:40.5	43.4±11.7	-13.89	-0.55	0.181	42.07	18.93	1.35	0.43	NELG	<21.89
84	CXOMP	J105626.7-033721	10:56:26.77	-03:37:21.3	78.9±11.5	-13.65	+0.33	0.643	43.60	21.26	2.62	1.04	ALG	23.21 ^{+0.15} _{-0.13}
85	CXOMP	J105612.3-033501	10:56:12.37	-03:35:01.5	41.6±15.2	-13.89	-0.72	2.315	44.73	21.31	0.28	0.22	BLAGN	<22.56
86	CXOMP	J105643.1-034042	10:56:43.11	-03:40:42.2	127.5±12.4	-13.41	-0.78	2.118	45.11	18.15	0.27	0.27	BLAGN	<21.78
87	CXOMP	J105655.1-034322	10:56:55.10	-03:43:22.4	19.5± 5.8	-14.28	-0.77	4.050	44.92	22.35	2.22	0.32	BLAGN	<22.70
88	CXOMP	J105659.4-034716	10:56:59.43	-03:47:15.5	59.8±10.6	-13.77	-0.59	1.784	44.57	22.27	1.58	0.80	BLAGN	22.46 ^{+0.18} _{-0.20}
89	CXOMP	J105646.5-034707	10:56:46.38	-03:47:08.4	17.6± 8.6	-14.29	-0.75	2.248	44.30	22.05	0.06	0.09	BLAGN	<22.64
90	CXOMP	J105655.5-034030	10:56:55.59	-03:40:30.1	33.0± 7.0	-14.06	-0.79	0.698	43.27	21.29	0.87	0.58	BLAGN	<21.20
91	CXOMP	J105646.4-033905	10:56:46.47	-03:39:05.5	30.3± 6.7	-14.09	-0.73	1.250	43.87	21.87	0.44	0.20	BLAGN	<21.56
92	CXOMP	J105700.0-033445	10:57:00.06	-03:34:45.6	14.9± 5.9	-14.39	-0.65	1.177	43.50	22.07	0.71	0.24	BLAGN	<22.02
93	CXOMP	J105650.6-033508	10:56:50.63	-03:35:08.2	16.4± 5.9	-14.36	-0.83	0.818	43.14	21.93	0.97	0.67	BLAGN	<20.63
94	CXOMP	J105641.2-033853	10:56:41.29	-03:38:53.2	9.9± 4.7	-14.56	-0.69	2.697	44.21	21.24	0.25	0.12	BLAGN	<22.82
95	CXOMP	J114215.1+660548	11:42:15.19	+66:05:48.4	38.2±11.3	-14.09	+0.31	0.414	42.70	20.75	2.26	0.67	NELG	22.73 ^{+0.18} _{-0.18}
96	CXOMP	J114044.3+660311	11:40:44.31	+66:03:11.8	59.3± 9.1	-13.94	-0.68	2.310	44.67	20.56	0.10	0.16	BLAGN	<22.06
97	CXOMP	J114028.0+660320	11:40:28.01	+66:03:20.1	22.6± 6.4	-14.34	-0.62	1.957	44.10	21.64	1.31	0.34	BLAGN	<21.97
98	CXOMP	J114021.9+660428	11:40:21.99	+66:04:28.8	35.0± 7.3	-14.17	-0.69	1.413	43.92	21.27	0.56	-0.12	BLAGN	<21.99
99	CXOMP	J114024.6+660215	11:40:24.60	+66:02:15.8	47.4± 8.8	-14.03	-0.62	1.710	44.26	21.22	0.39	0.54	BLAGN	<22.05
100	CXOMP	J114022.0+660028	11:40:22.00	+66:00:28.4	37.4± 9.4	-14.12	-0.72	1.834	44.25	21.30	0.57	0.20	BLAGN	<21.83
101	CXOMP	J114018.5+660111	11:40:18.55	+66:01:11.1	21.7± 7.9	-14.36	-0.67	1.270	43.61	21.12	0.57	0.36	BLAGN	<21.32
102	CXOMP	J113950.1+660025	11:39:50.17	+66:00:25.0	55.8±12.9	-13.93	-0.64	0.858	43.62	21.64	0.51	0.64	BLAGN	<21.73
103	CXOMP	J114124.3+660921	11:41:24.39	+66:09:21.5	61.8± 9.2	-13.90	-0.80	1.088	43.91	19.89	0.28	0.00	BLAGN	<20.43
104	CXOMP	J114046.4+660913	11:40:46.45	+66:09:13.0	16.3± 5.3	-14.44	-0.67	1.933	43.99	21.72	0.03	0.42	BLAGN	<22.21

X-ray survey of AGN with Chandra

TABLE 5
HARD AGN^a

105	CXOMP	J114031.1+660858	11:40:31.15	+66:08:58.2	198.1±15.2	-13.41	-0.65	1.269	44.56	21.02	0.77	0.21	BLAGN	<21.56
106	CXOMP	J114001.9+660642	11:40:01.95	+66:06:42.3	29.2± 7.3	-14.24	-0.64	0.481	42.70	20.25	2.19	0.77	NELG	<21.46
107	CXOMP	J114036.2+661317	11:40:36.22	+66:13:17.4	22.7± 7.7	-14.32	-0.72	3.337	44.68	21.57	0.04	0.10	BLAGN	<22.56
108	CXOMP	J113944.5+661137	11:39:44.58	+66:11:37.1	66.4±11.7	-13.83	-0.66	2.113	44.69	20.00	0.98	0.26	BLAGN	<21.69
109	CXOMP	J113941.2+661319	11:39:41.29	+66:13:19.6	34.7±12.4	-14.11	-0.56	0.495	42.86	20.76	2.04	0.71	ALG	<21.82
110	CXOMP	J114022.0+660816	11:40:22.00	+66:08:16.3	24.8± 7.2	-14.30	-0.44	0.786	43.16	20.37	3.20	1.42	ALG	<21.70
111	CXOMP	J134411.0+555353	13:44:11.06	+55:53:53.0	12.1± 4.8	-14.21	-0.71	0.470	42.71	20.49	2.30	0.51	NELG	<21.76
112	CXOMP	J134359.1+555259	13:43:59.14	+55:52:59.6	24.1± 6.6	-13.88	>0.34	0.593	43.28	20.67	2.59	0.60	NELG	23.32 ^{+0.22} _{-0.24}
113	CXOMP	J134450.6+555531	13:44:50.62	+55:55:31.9	25.7± 6.3	-13.90	-0.51	1.784	44.44	20.44	0.35	0.25	BLAGN	22.63 ^{+0.19} _{-0.20}
114	CXOMP	J134440.2+555648	13:44:40.21	+55:56:48.4	56.0± 8.6	-13.55	-0.78	1.156	44.32	19.05	0.27	0.04	BLAGN	<21.14
115	CXOMP	J134508.0+555058	13:45:08.06	+55:50:58.6	15.9± 5.6	-14.11	-0.65	0.608	43.08	21.08	1.60	0.55	NELG	<21.51
116	CXOMP	J141656.1+444720	14:16:56.18	+44:47:20.3	63.1± 9.1	-13.33	-0.48	0.469	43.58	21.31	2.37	0.74	BLAGN	21.77 ^{+0.15} _{-0.16}
117	CXOMP	J141747.4+444544	14:17:47.48	+44:45:44.9	18.8± 9.4	-13.79	-0.13	2.138	44.75	19.92	0.34	0.15	BLAGN	<22.42
118	CXOMP	J141703.7+443851	14:17:03.74	+44:38:51.1	26.0± 8.8	-13.58	-0.74	1.600	44.64	19.43	0.56	0.26	BLAGN	<21.92
119	CXOMP	J141624.9+444045	14:16:24.74	+44:40:45.2	35.6± 8.4	-13.54	-0.48	1.440	44.57	20.78	0.82	0.10	BLAGN	<21.60
120	CXOMP	J141700.7+445606	14:17:00.77	+44:56:06.9	575.5±25.4	-12.30	-0.77	0.114	43.22	15.93	0.18	0.15	BLAGN	<18.99
121	CXOMP	J141656.3+445340	14:16:56.34	+44:53:40.2	26.5± 6.6	-13.67	+0.25	0.440	43.18	19.28	1.85	0.50	NELG	22.80 ^{+0.15} _{-0.18}
122	CXOMP	J141655.6+445453	14:16:55.62	+44:54:53.1	25.6± 6.8	-13.68	-0.58	0.579	43.46	20.86	2.00	0.53	ALG	21.87 ^{+0.30} _{-0.23}
123	CXOMP	J141715.0+445316	14:17:15.08	+44:53:17.1	15.1± 5.9	-13.91	-0.73	2.449	44.77	19.62	-0.01	0.03	BLAGN	<22.02
124	CXOMP	J141637.0+444645	14:16:37.08	+44:46:45.6	46.6± 7.9	-13.47	-0.72	0.394	43.27	20.02	0.60	0.23	BLAGN	<20.33
125	CXOMP	J141624.5+445156	14:16:24.52	+44:51:56.7	37.7± 7.4	-13.51	-0.70	2.015	44.96	18.16	0.32	-0.23	BLAGN	<22.44
126	CXOMP	J141626.6+445240	14:16:26.69	+44:52:40.2	26.9± 6.6	-13.67	-0.46	0.675	43.63	20.27	1.55	0.76	BLAGN	<21.53
127	CXOMP	J141558.7+445009	14:15:58.79	+44:50:09.4	29.9± 7.9	-13.61	-0.64	1.364	44.44	19.97	0.19	-0.16	BLAGN	<21.17
128	CXOMP	J171758.4+671203	17:17:58.47	+67:12:03.1	45.2± 8.2	-13.69	-0.62	1.800	44.66	21.05	0.25	0.26	BLAGN	<21.84
129	CXOMP	J171740.6+671147	17:17:40.63	+67:11:47.2	12.3± 4.8	-14.29	-0.57	2.318	44.33	21.97	-0.24	-0.23	BLAGN	<22.11
130	CXOMP	J171837.7+671351	17:18:37.76	+67:13:51.4	20.0± 9.3	-14.03	-0.58	1.550	44.16	20.84	1.03	0.40	BLAGN	<22.19
131	CXOMP	J171748.3+670544	17:17:48.31	+67:05:44.9	27.7± 7.6	-13.89	-0.69	0.482	43.05	19.86	0.35	0.12	BLAGN	<21.15
132	CXOMP	J171635.5+671626	17:16:35.56	+67:16:26.0	21.7± 6.1	-13.98	-0.52	0.505	43.01	20.43	1.97	0.48	ALG	<21.70
133	CXOMP	J171636.9+670829	17:16:36.90	+67:08:29.7	56.2± 8.7	-13.59	+0.51	0.795	43.88	22.38	2.75	1.08	NELG	23.20 ^{+0.14} _{-0.14}
134	CXOMP	J171700.7+670519	17:17:00.70	+67:05:19.7	27.1± 7.0	-13.90	-0.63	1.155	43.97	20.72	0.30	0.01	BLAGN	<21.31
135	CXOMP	J184514.8+795010	18:45:14.81	+79:50:10.0	18.1± 7.7	-13.83	-0.58	1.107	44.00	20.36	0.52	-0.03	BLAGN	<21.99
136	CXOMP	J205648.1-042937	20:56:48.11	-04:29:37.9	34.4± 9.0	-13.73	-0.49	0.172	42.18	18.72	1.73	0.57	NELG	<21.74
137	CXOMP	J205624.8-042824	20:56:24.84	-04:28:24.4	10.1± 5.0	-14.23	-0.58	1.511	43.93	22.13	0.52	0.33	BLAGN	<21.68
138	CXOMP	J205632.8-042650	20:56:32.83	-04:26:50.4	21.0± 7.5	-13.95	-0.52	1.511	44.22	20.18	0.97	0.50	BLAGN	<21.95
139	CXOMP	J205638.1-043753	20:56:38.15	-04:37:53.2	25.6± 6.6	-13.85	-0.54	2.970	45.03	19.70	0.50	0.11	BLAGN	<22.66
140	CXOMP	J205641.9-043300	20:56:41.98	-04:33:00.7	19.4± 6.1	-13.99	>0.48	0.467	42.92	20.91	2.18	0.69	NELG	23.22 ^{+0.29} _{-0.31}
141	CXOMP	J205620.5-043059	20:56:20.52	-04:30:59.5	8.3± 4.1	-14.36	-0.68	2.335	44.27	21.17	-0.08	0.01	BLAGN	<22.44
142	CXOMP	J205603.6-043118	20:56:03.61	-04:31:18.0	14.8± 5.2	-14.08	-0.66	1.010	43.65	21.12	0.37	0.11	BLAGN	<21.25
143	CXOMP	J205629.1-043415	20:56:29.15	-04:34:15.8	8.7± 4.1	-14.35	-0.74	1.031	43.40	21.42	0.89	0.44	BLAGN	<21.32
144	CXOMP	J205624.7-043533	20:56:24.77	-04:35:33.8	41.4± 7.5	-13.68	>0.73	0.261	42.64	19.48	1.73	0.56	NELG	23.18 ^{+0.17} _{-0.19}
145	CXOMP	J205618.6-043429	20:56:18.68	-04:34:29.0	35.4± 7.1	-13.73	+0.51	0.527	43.31	21.59	2.78	1.01	NELG	23.10 ^{+0.14} _{-0.14}
146	CXOMP	J205606.6-043725	20:56:06.64	-04:37:25.1	14.5± 5.1	-14.11	-0.76	1.188	43.79	19.93	0.56	0.23	BLAGN	<21.37
147	CXOMP	J205609.3-043832	20:56:09.38	-04:38:32.2	13.9± 5.1	-14.12	-0.24	0.396	42.62	20.91	2.70	0.84	ALG	<21.93
148	CXOMP	J205608.9-043538	20:56:08.93	-04:35:38.6	8.4± 4.1	-14.36	>0.08	1.436	43.75	21.25	0.57	0.18	BLAGN	<23.19
149	CXOMP	J205605.4-044057	20:56:05.47	-04:40:57.5	34.2± 7.7	-13.68	-0.47	0.799	43.80	21.20	0.73	0.52	BLAGN	<21.92
150	CXOMP	J205603.0-043613	20:56:03.03	-04:36:13.4	10.8± 4.7	-14.24	-0.07	0.469	42.68	20.83	2.75	0.94	NELG	22.43 ^{+0.22} _{-0.30}
151	CXOMP	J205614.8-044134	20:56:14.83	-04:41:34.8	12.8± 5.7	-14.13	-0.62	2.476	44.56	21.95	0.67	0.11	BLAGN	<22.71
152	CXOMP	J205602.0-043644	20:56:02.00	-04:36:44.8	14.3± 5.2	-14.11	>0.42	0.466	42.80	21.74	3.12	0.98	NELG	23.78 ^{+0.27} _{-0.34}
153	CXOMP	J213924.9-234221	21:39:24.91	-23:42:21.8	33.0±11.4	-13.68	-0.43	0.401	43.08	19.73	2.12	0.50	NELG	<22.35
154	CXOMP	J214041.4-234719	21:40:41.47	-23:47:19.9	255.3±17.9	-12.80	-0.75	0.491	44.17	18.36	0.11	0.12	BLAGN	<20.65
155	CXOMP	J214018.0-234920	21:40:18.01	-23:49:20.1	17.3± 7.7	-13.98	-0.85	1.406	44.11	19.62	0.28	-0.03	BLAGN	<21.71
156	CXOMP	J214019.1-234837	21:40:19.10	-23:48:37.7	24.9± 7.6	-13.83	+0.01	0.387	42.88	21.59	1.79	0.43	NELG	22.83 ^{+0.14} _{-0.15}
157	CXOMP	J214018.3-234055	21:40:18.32	-23:40:55.9	14.7± 5.1	-13.99	-0.83	1.648	44.27	19.52	0.29	0.15	BLAGN	<21.53

TABLE 5
HARD AGN^a

158	CXOMP	J214010.4-233905	21:40:10.49	-23:39:05.1	27.8± 6.5	-13.70	>0.60	0.453	43.18	20.66	2.33	0.58	NELG	23.37 ^{+0.19} _{-0.25}
159	CXOMP	J214001.4-234112	21:40:01.42	-23:41:12.8	88.5±10.5	-13.16	-0.75	0.188	42.84	18.52	1.40	0.40	NELG	<20.57
160	CXOMP	J224007.1+031813	22:40:07.11	+03:18:13.3	84.9±10.4	-13.15	-0.72	0.528	43.89	18.96	0.81	0.48	BLAGN	<20.54
161	CXOMP	J224022.8+032451	22:40:22.83	+03:24:51.3	22.4± 6.0	-13.67	-0.71	0.679	43.64	19.92	0.52	0.42	BLAGN	<21.07
162	CXOMP	J230257.3+084834	23:02:57.37	+08:48:34.8	82.0±10.3	-13.76	-0.60	1.974	44.69	18.96	0.34	0.33	BLAGN	<22.07
163	CXOMP	J230252.2+084810	23:02:52.22	+08:48:10.9	24.3± 6.2	-14.27	-0.65	1.407	43.81	21.20	0.41	0.18	BLAGN	<21.85
164	CXOMP	J230252.1+085520	23:02:52.17	+08:55:20.9	24.6±11.6	-14.23	-0.46	3.757	44.90	20.37	1.70	0.25	BLAGN	<23.72
165	CXOMP	J230250.9+085311	23:02:50.91	+08:53:11.6	23.6± 9.0	-14.27	-0.05	0.453	42.61	20.21	2.11	0.64	ALG	22.27 ^{+0.20} _{-0.28}
166	CXOMP	J230300.9+084659	23:03:00.98	+08:46:59.6	261.6±17.3	-13.24	-0.47	0.738	44.15	21.88	1.34	0.66	BLAGN	21.59 ^{+0.14} _{-0.16}
167	CXOMP	J230314.5+084845	23:03:14.50	+08:48:45.0	89.4±12.2	-13.68	>0.74	0.229	42.51	19.70	2.00	0.67	ALG	23.29 ^{+0.18} _{-0.20}
168	CXOMP	J230304.6+084130	23:03:04.60	+08:41:30.4	12.7± 5.7	-14.51	-0.61	2.592	44.22	22.06	0.21	0.10	BLAGN	<22.45
169 ^e	CXOMP	J230246.0+084523	23:02:46.05	+08:45:23.8	109.3±11.5	-13.20	-0.46	1.944	45.23	19.08	0.51	0.55	BLAGN	...
170	CXOMP	J230221.6+084653	23:02:21.66	+08:46:53.0	63.1± 9.9	-13.82	-0.36	0.680	43.48	21.78	1.47	0.66	NELG	21.98 ^{+0.17} _{-0.18}
171	CXOMP	J230218.0+084409	23:02:18.09	+08:44:09.4	30.8± 8.3	-14.13	-0.65	0.988	43.57	20.38	0.39	0.16	BLAGN	<21.37
172	CXOMP	J230204.1+084654	23:02:04.18	+08:46:54.8	54.8±13.7	-13.84	-0.46	0.230	42.35	18.43	1.67	0.62	NELG	<21.77
173	CXOMP	J230211.1+084654	23:02:11.13	+08:46:57.6	27.7±10.0	-14.16	-0.18	2.570	44.57	21.35	0.30	0.07	BLAGN	23.34 ^{+0.29} _{-0.40}
174	CXOMP	J230254.3+083904	23:02:54.38	+08:39:04.9	462.9±22.9	-12.99	-0.57	0.437	43.85	19.00	0.91	0.46	BLAGN	21.24 ^{+0.11} _{-0.14}
175	CXOMP	J230243.0+083946	23:02:43.01	+08:39:46.7	47.3± 8.6	-13.98	-0.53	0.438	42.86	19.26	2.31	0.74	ALG	<21.69
176	CXOMP	J230240.2+083611	23:02:40.21	+08:36:11.1	265.0±19.0	-13.20	-0.53	1.957	45.24	20.76	0.67	0.60	BLAGN	22.20 ^{+0.12} _{-0.13}
177	CXOMP	J234849.7+010716	23:48:49.77	+01:07:16.2	28.3±10.7	-13.76	-0.61	1.660	44.50	20.01	0.42	0.23	BLAGN	<21.81
178	CXOMP	J234812.8+010022	23:48:12.89	+01:00:22.3	29.6± 6.5	-13.89	-0.74	0.718	43.48	20.95	0.90	0.50	BLAGN	<21.31
179	CXOMP	J234826.2+010330	23:48:26.26	+01:03:30.7	67.5± 9.5	-13.51	-0.74	2.174	45.04	20.92	0.23	0.21	BLAGN	<22.01
180	CXOMP	J234823.2+010357	23:48:23.26	+01:03:57.8	13.9± 5.3	-14.20	-0.77	2.234	44.38	21.40	-0.11	0.02	BLAGN	<22.26
181	CXOMP	J234810.5+010552	23:48:10.54	+01:05:51.9	27.9± 7.5	-13.88	-0.73	1.859	44.51	19.31	0.32	0.16	BLAGN	<22.33
182	CXOMP	J234752.5+010306	23:47:52.55	+01:03:06.8	15.0± 6.5	-14.10	-0.51	2.411	44.56	20.60	0.36	0.05	BLAGN	<22.74
183	CXOMP	J234835.3+005832	23:48:35.33	+00:58:32.6	84.0±10.5	-13.52	-0.72	0.946	44.14	20.87	0.38	0.13	BLAGN	<21.37
184	CXOMP	J234820.8+010024	23:48:20.82	+01:00:24.2	51.0± 8.3	-13.80	-0.75	1.210	44.12	21.31	0.79	0.09	BLAGN	<21.07
185	CXOMP	J234818.9+005950	23:48:18.94	+00:59:50.1	27.3± 6.5	-14.08	-0.77	1.937	44.35	22.14	0.33	0.24	BLAGN	<21.55
186	CXOMP	J234813.7+005640	23:48:13.76	+00:56:40.0	10.0± 4.6	-14.51	-0.11	1.042	43.25	20.37	0.57	0.09	BLAGN	23.16 ^{+0.27} _{-0.36}
187	CXOMP	J234811.5+005700	23:48:11.54	+00:57:00.4	23.7± 6.1	-14.13	-0.82	1.815	44.23	21.74	0.57	0.42	BLAGN	<21.16
188	CXOMP	J234820.2+005437	23:48:20.21	+00:54:37.3	44.0± 8.1	-13.88	+0.21	0.279	42.51	19.33	1.52	0.46	NELG	22.60 ^{+0.11} _{-0.13}

^a [The complete version of this table is in the electronic edition of the Journal. The printed edition contains only a sample].^b observed frame; 2.5-8.0 keV; background subtracted^c galactic absorption-corrected; observed frame; 2.0-8.0 keV; units of erg cm⁻² s⁻¹^d rest frame; 2.0-8.0 keV; units of erg s⁻¹^e Source fell near the chip gap. No spectral fitting is performed.

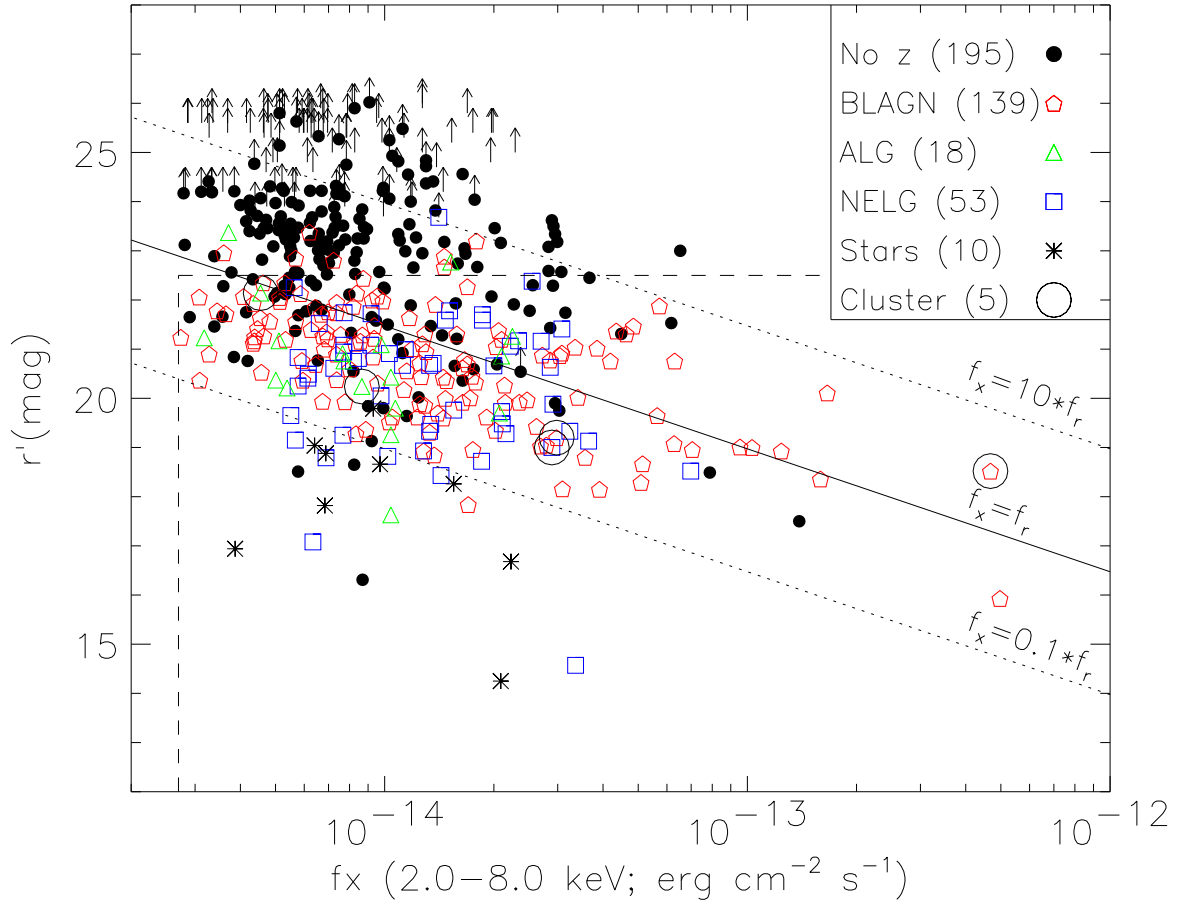


FIG. 1.— X-ray flux (2–8 keV) vs. optical magnitude (r'). Optical spectroscopic classifications are indicated (top right box) with the sample size in parenthesis. X-ray sources with no optical counter-parts are shown by an arrow placed at the hypothetical magnitude for a 5σ detection from our optical imaging (Table 2). The dashed vertical and horizontal lines mark the X-ray flux limit and optical magnitude limit for the subsequent analysis. The slanted lines mark the f_x/f_r ratios of 0.1, 1, 10.

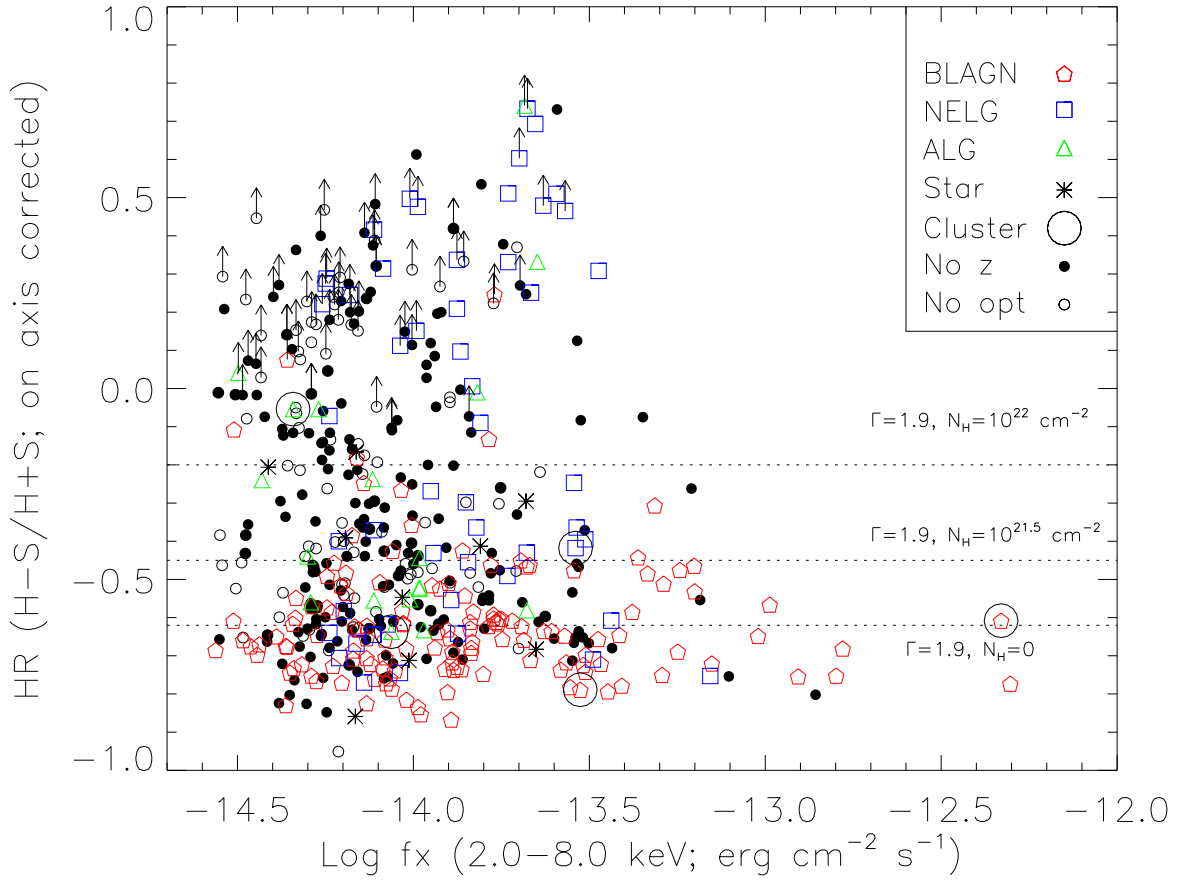


FIG. 2.— X-ray hardness ratio (HR) as a function of 2.0–8.0 keV flux. The hardness ratio has been recalculated to the equivalent on-axis value for all sources. Error bars have been omitted for clarity and lower limits are marked by an arrow. Symbol type indicates the spectroscopic classification. Objects with no spectrum are marked as filled circles, while objects with no optical counterpart are marked by a small open circle.

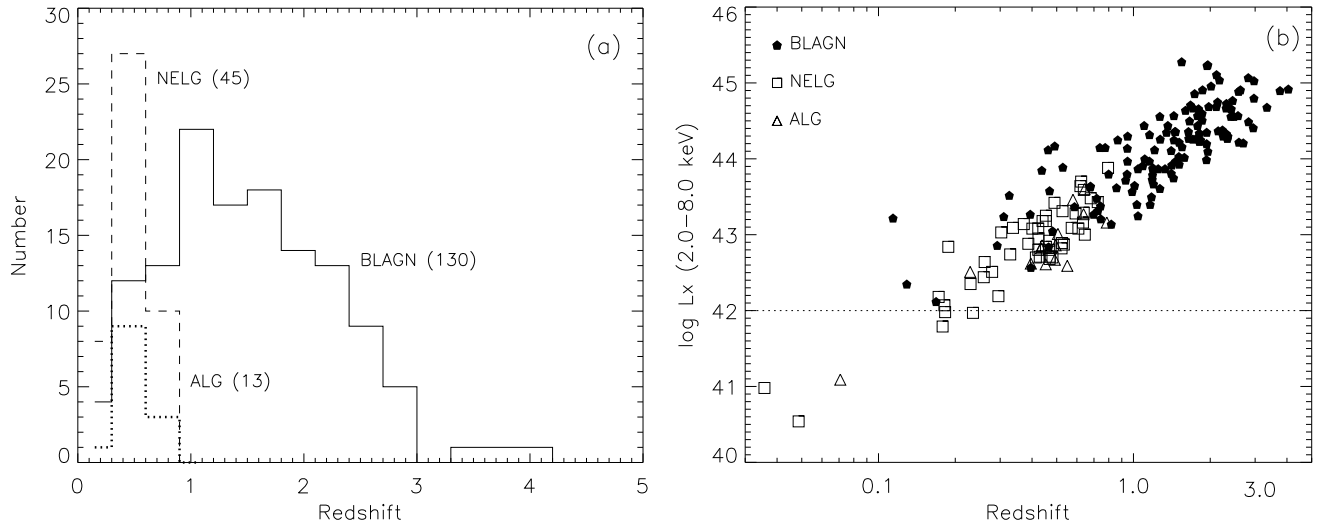


FIG. 3.— (a) Redshift distribution of hard band detected AGN with $L_{2.0-8.0\text{keV}} > 10^{42} \text{ erg s}^{-1}$. (b) X-ray luminosity, redshift distribution. The horizontal, dashed line marks our chosen minimum luminosity required for AGN selection. All but one NELG ($z = 0.014$; $\log(L_{2.0-8.0\text{keV}}) = 39.5$) are shown.

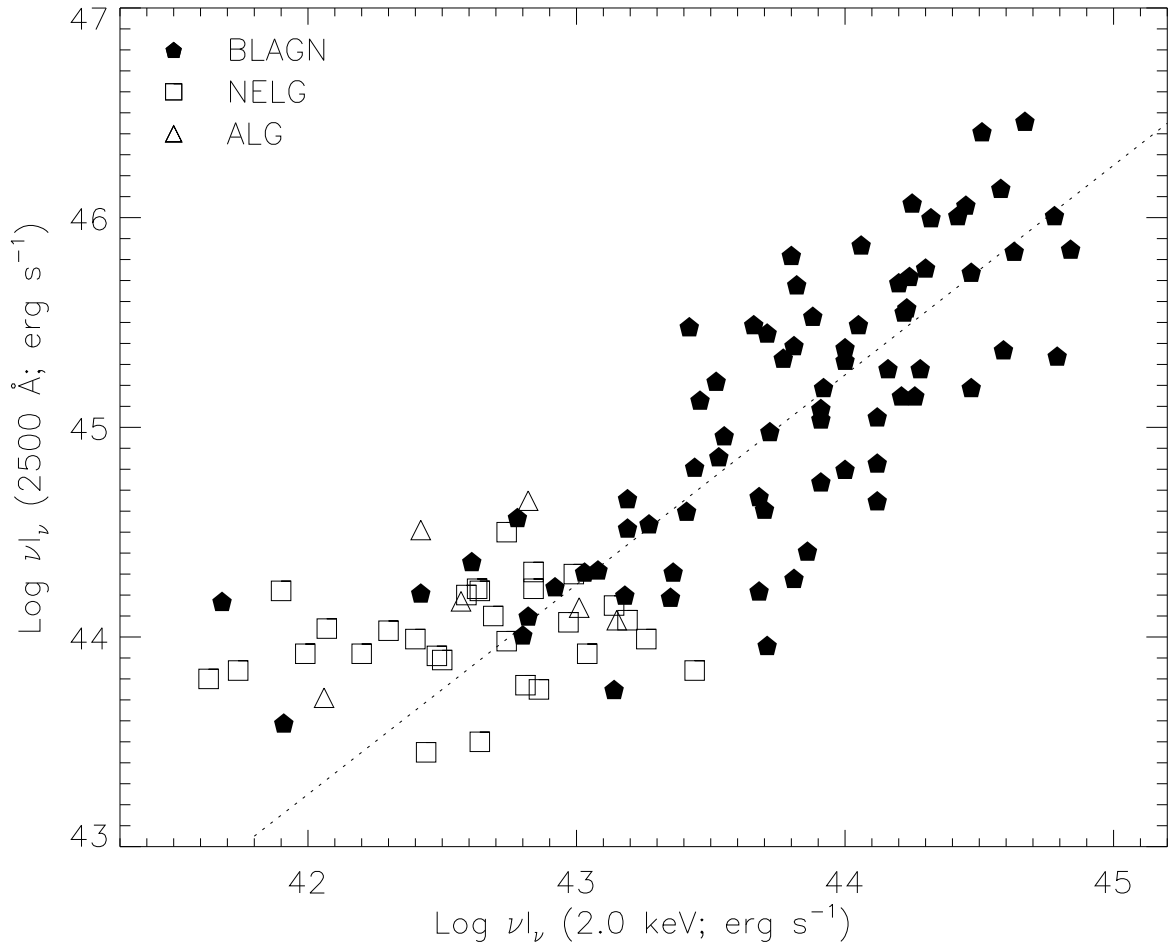


FIG. 4.— X-ray versus optical luminosity. The dashed line is the mean X-ray to optical flux ratio ($\langle \alpha_{OX} \rangle = 1.48$) of the BLAGN with $\log L_{2.0-8.0\text{keV}} > 43.5$ (units of erg s^{-1}). Propagating typical errors in a Monte-Carlo simulation for each object yields error bars of similar size to the points shown here.

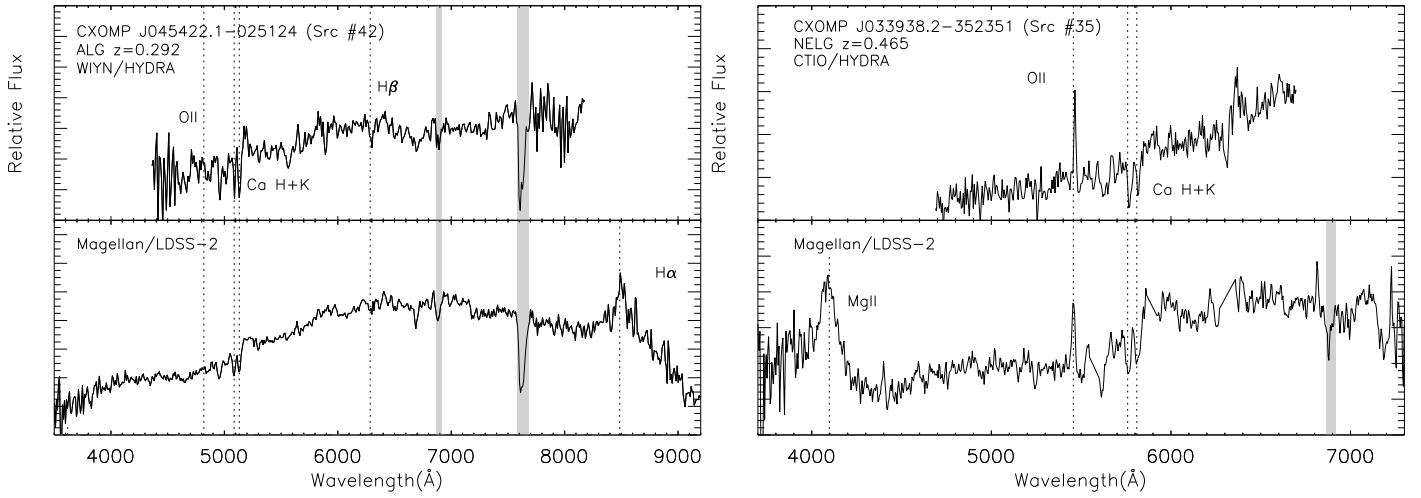


FIG. 5.— Complexity of object classification. Two optical spectra of each source were acquired with slightly different wavelength coverage. The spectra taken with Magellan clearly reveal a broad emission line in each case. Shaded regions mark the uncorrected telluric O_2 absorption features. Dashed lines mark the expected observed wavelengths of emission or absorption features at the source redshift.

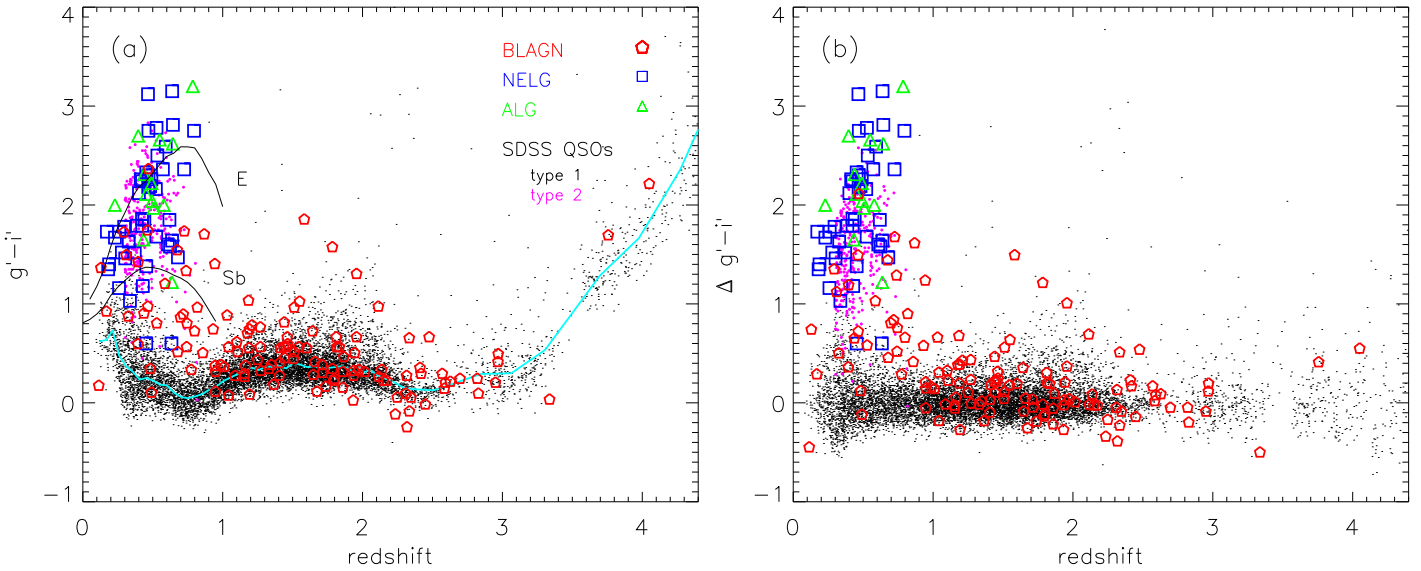


FIG. 6.— (a) Optical color of ChaMP hard AGN compared with type 1 (Schneider et al. 2003) and type 2 (Zakamska et al. 2003) SDSS quasars. The median type 1 SDSS quasar color in redshift bins of 0.05 ($z < 2.2$), 0.2 ($2.2 < z < 2.6$) and 0.3 ($z > 2.6$) is shown by the cyan curve. (b) Color offsets from the median type 1 quasar color from the SDSS.

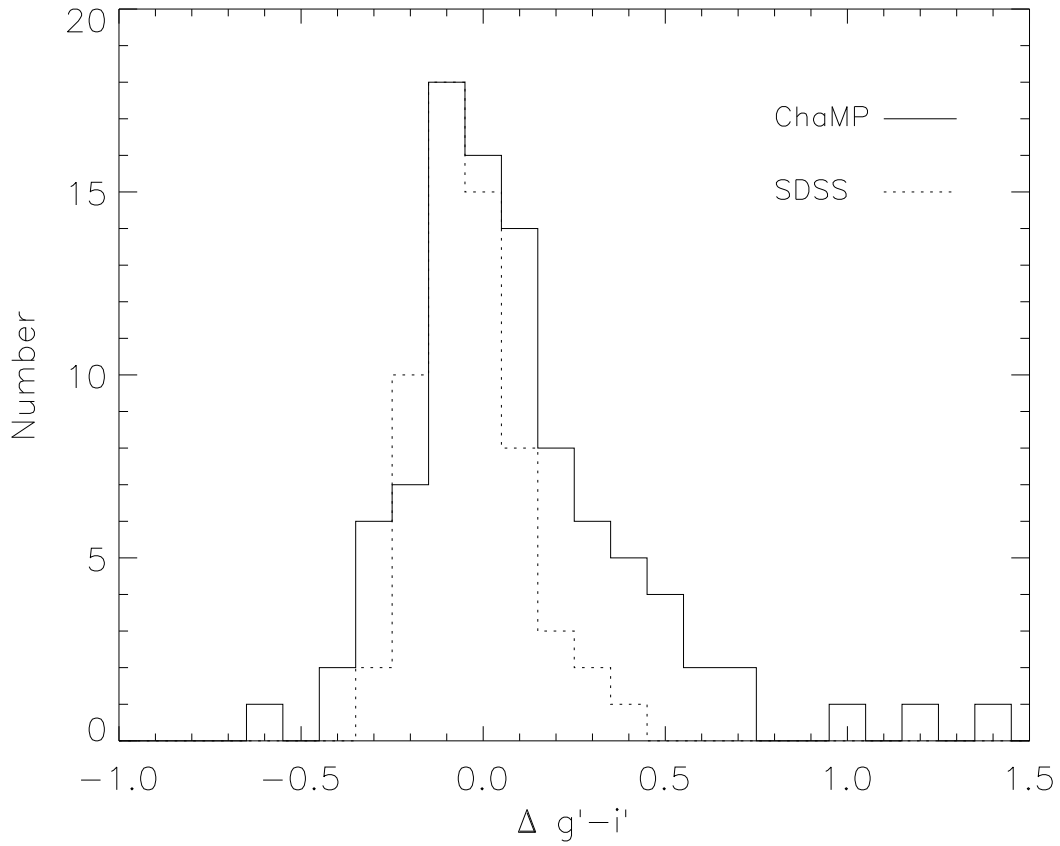


FIG. 7.— Color difference of ChaMP BLAGN and SDSS quasars with the median SDSS quasar color. A minimum redshift ($z > 1$) has been chosen to omit low luminosity AGN with a significant host component. The SDSS distribution has been normalized to match the peak of the ChaMP AGN.

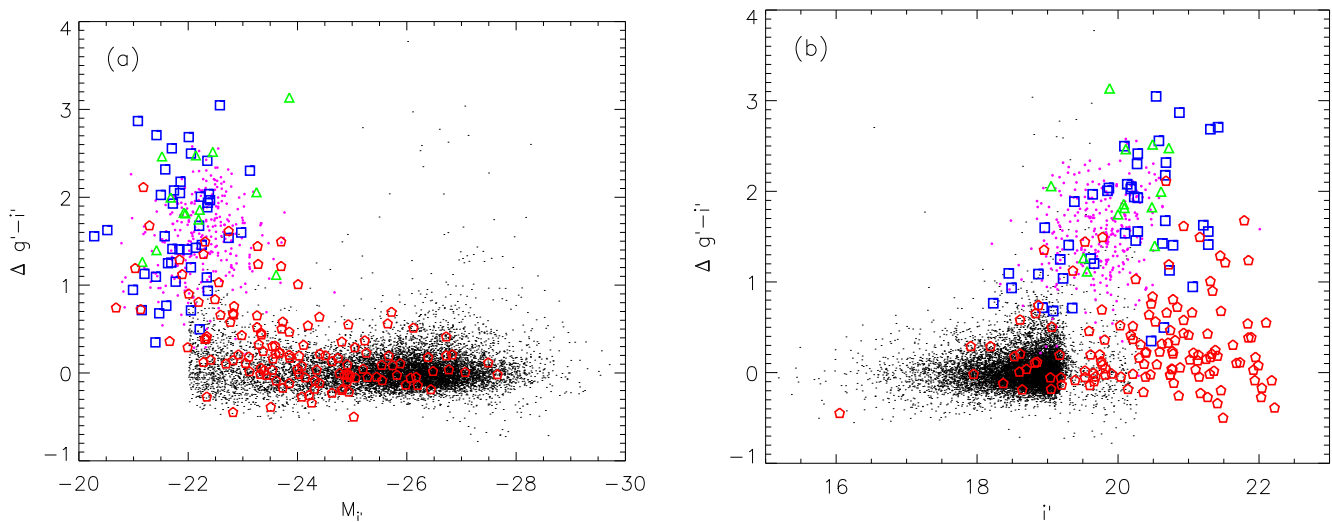


FIG. 8.— Optical color offset as a function of absolute magnitude M_r (a) and apparent magnitude i' (b). Same symbol types as Figure 6a.

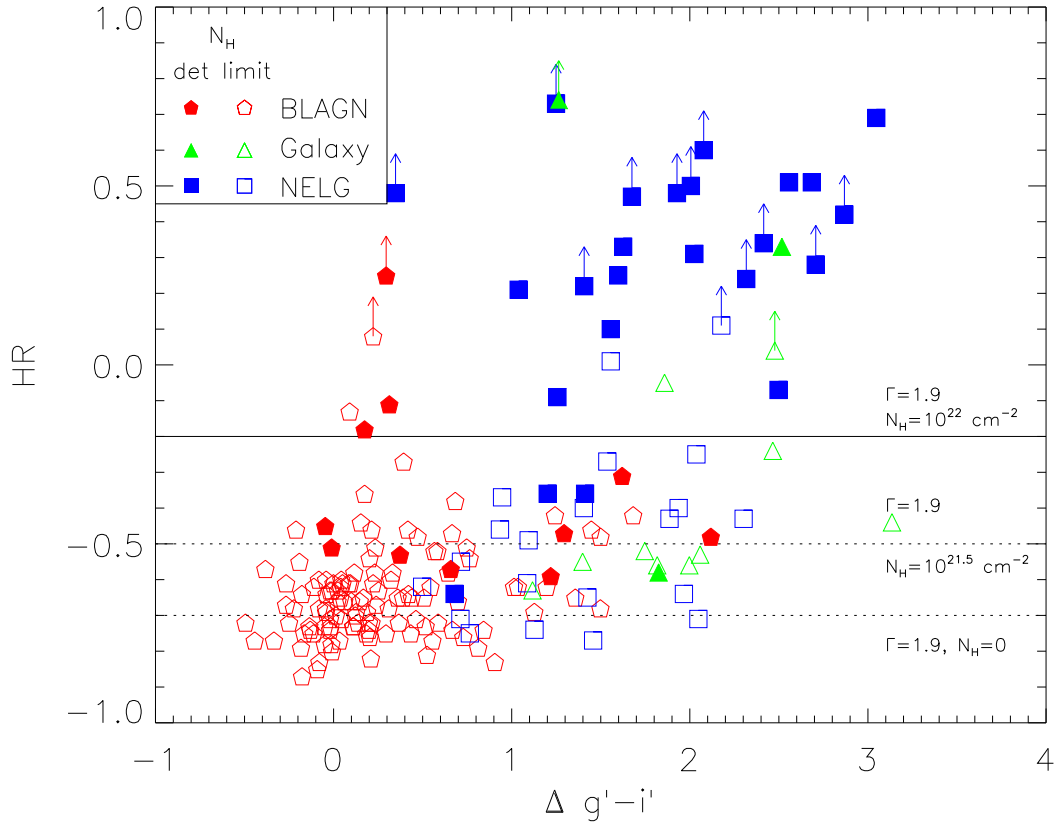


FIG. 9.— Hardness ratio vs. optical color. The horizontal lines mark the HR for a typical AGN with a powerlaw continuum ($\Gamma = 1.9$) absorbed by neutral gas intrinsic to the source. The solid line marks the division between unabsorbed and absorbed AGN as defined in this paper. The filled symbols mark the well constrained N_H measurements from X-ray spectral fits (Section 3.1) to compare with Figure 11.

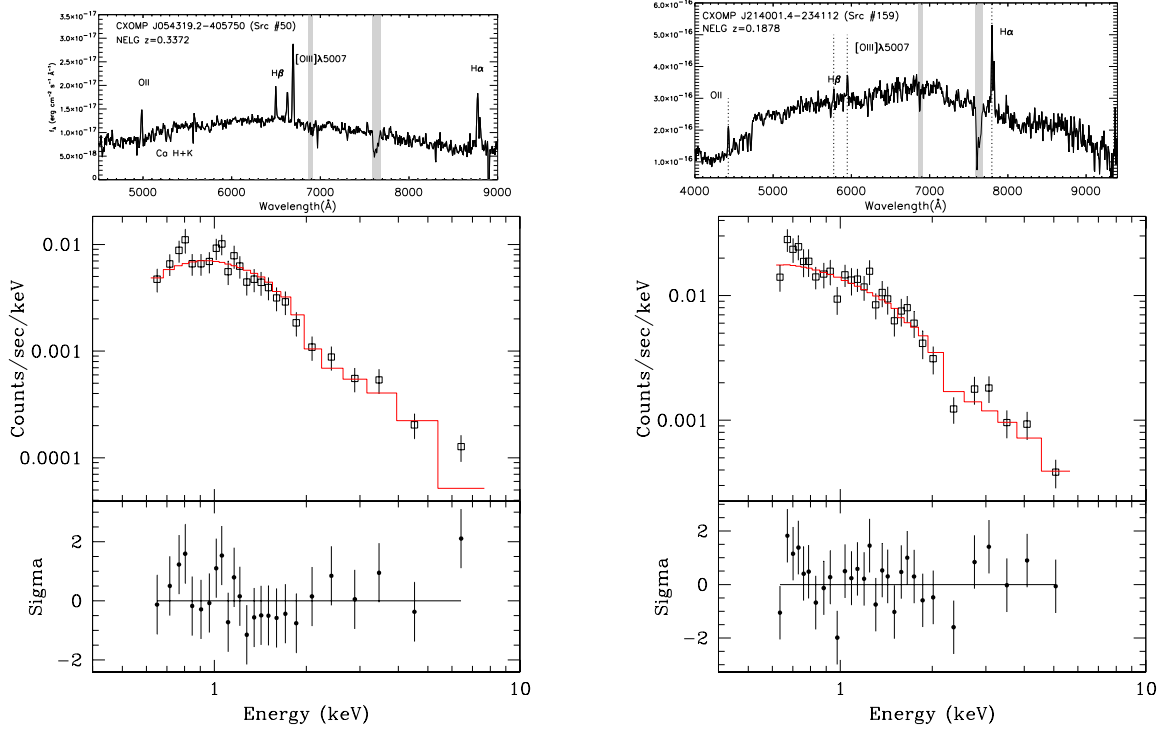


FIG. 10.— The X-ray and optical spectra of two X-ray unabsorbed, Narrow Emission Line Galaxies. Each column corresponds to one source. (top) Optical spectra, with shaded regions to mark the uncorrected atmospheric absorption features, are displayed. (Bottom) Best-fit absorbed powerlaw model (top panel) and residuals (bottom panel) are shown for each object.

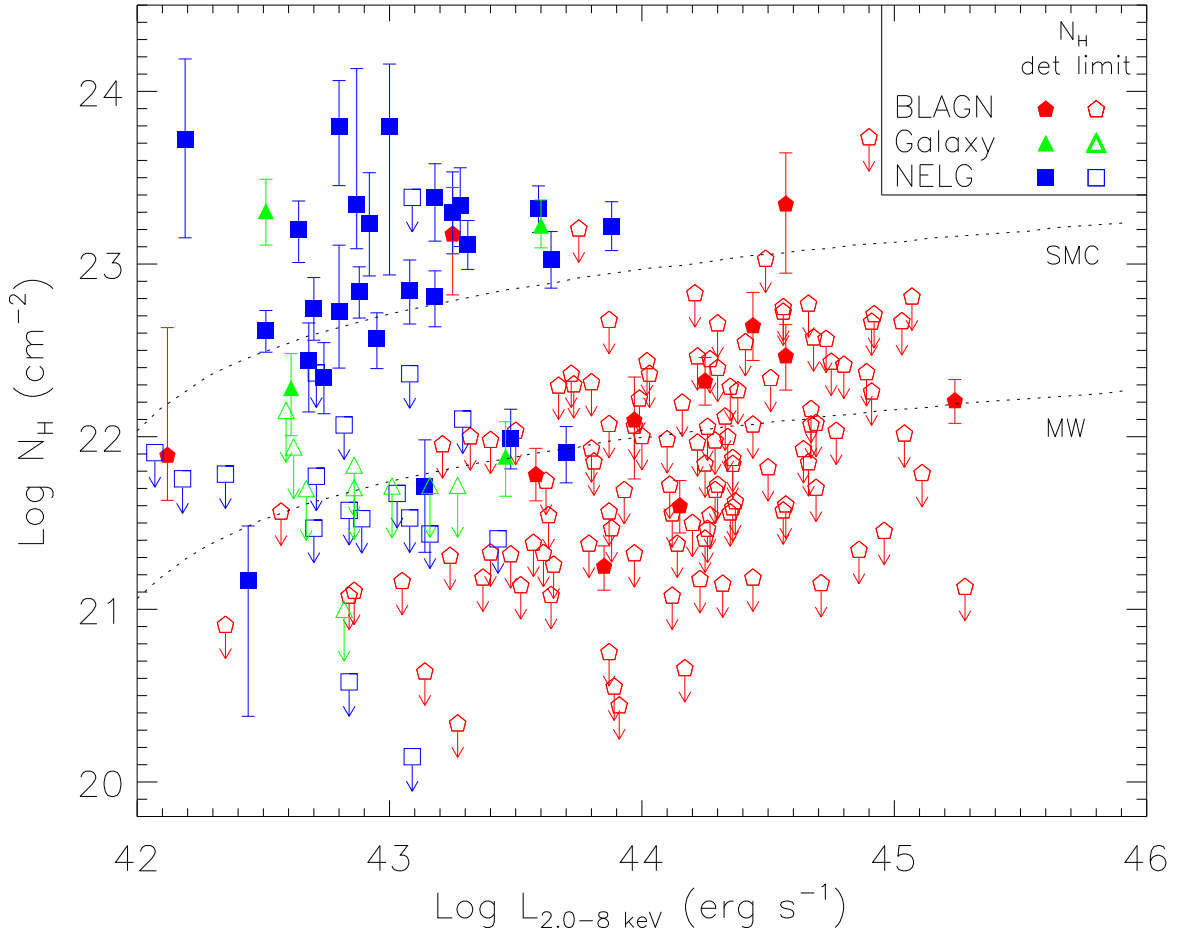


FIG. 11.— Luminosity vs. N_{H} . The X-ray luminosity has only been corrected for galactic absorption. Error bars represent 90% confidence intervals. The filled symbols mark the well constrained N_{H} measurements. Upper limits are shown with hollow symbols placed at the 90% value. The dashed lines mark our estimate of the absorbing column needed to hide optical emission from the broad line region for a given X-ray luminosity, assuming the average dust-to-gas ratio from Pei (1992) of the Milky Way (MW) and Small Magellanic Cloud (SMC).

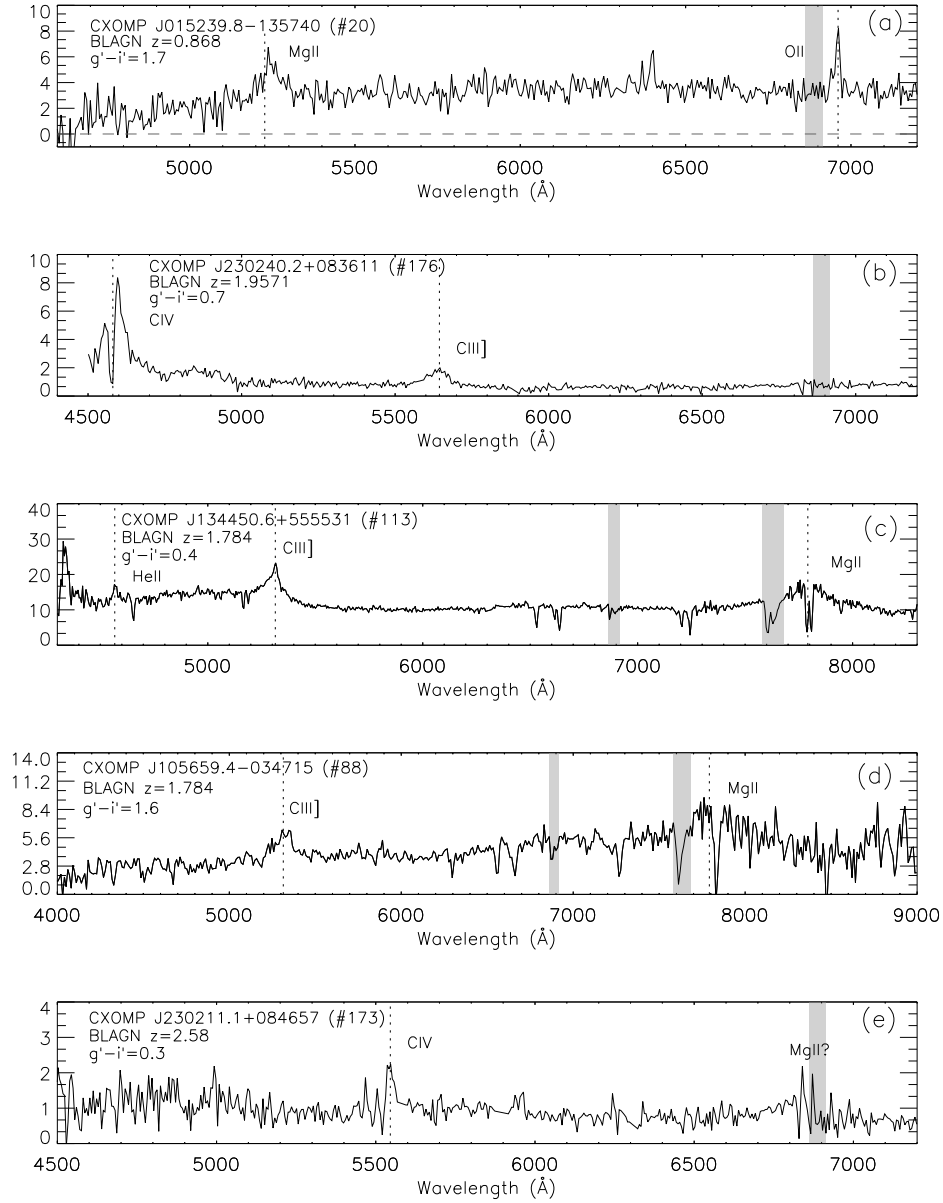


FIG. 12.— Optical spectra of X-ray absorbed quasars with $N_{\text{H}} > 10^{22} \text{ cm}^{-2}$ and rest frame $L_{2-8\text{keV}} > 10^{44} \text{ erg s}^{-1}$. The flux (f_λ ; y-axis) is in units of $10^{-17} \text{ erg cm}^{-2} \text{ s}^{-1} \text{ \AA}^{-1}$. Dashed lines show the spectral features at the redshift of the object. The optical color ($g' - i'$) is given. Shaded regions mark the uncorrected telluric O_2 absorption bands.

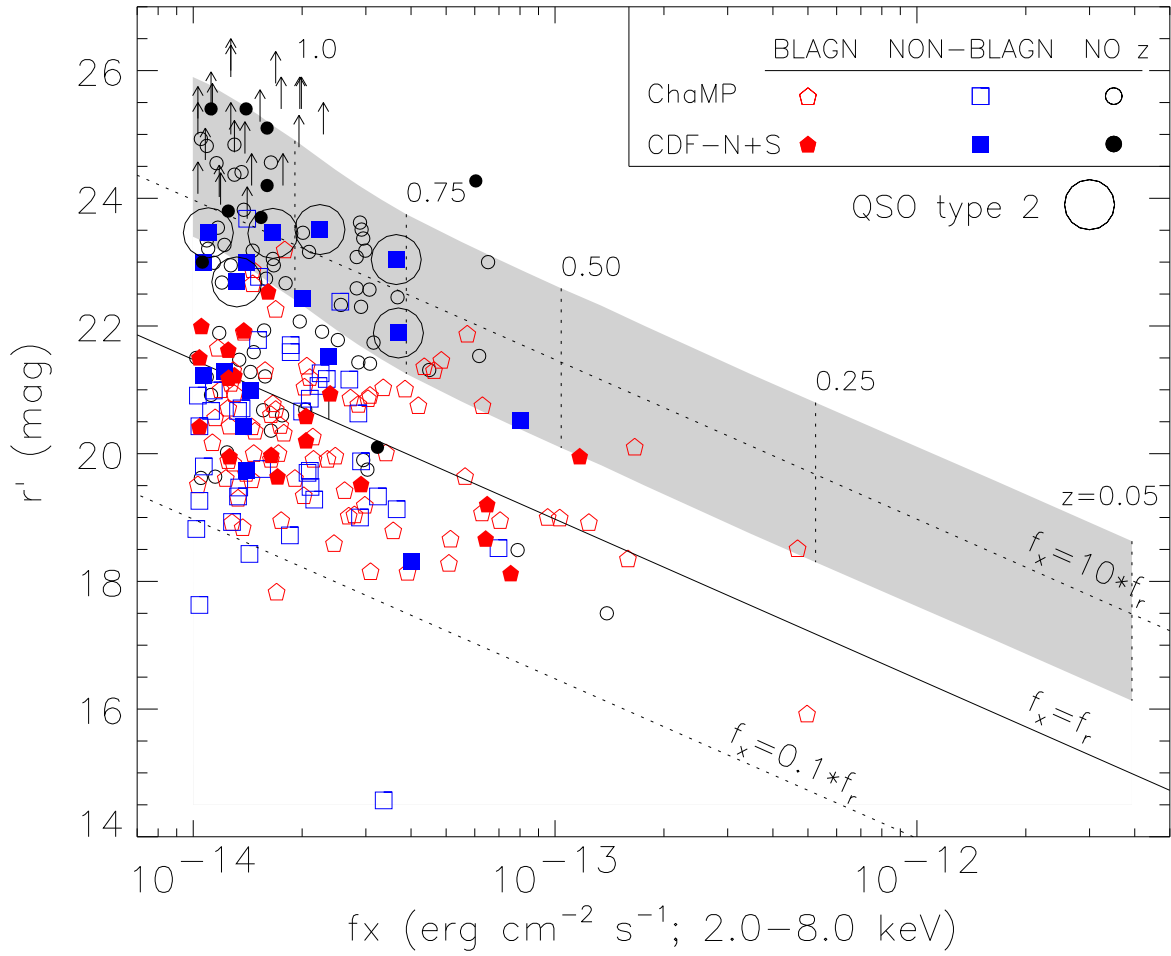


FIG. 13.— Where are the type 2 QSOs? The shaded region marks the location of a hypothetical, obscured QSO out to $z = 1.45$ as described in Section 7.5. We have included the sources from the *Chandra* Deep Fields which include 6 such quasars.